FACULTY
OF MATHEMATICS
AND PHYSICS
Charles University

MASTER THESIS

Bc. Martin Kaplan

Studies of the K-shell double vacancy production in the electron capture decays of ^{55}Fe, ^{54}Mn and ^{65}Zn using hybrid pixel detectors

Institute of Particle and Nuclear Physics

Supervisor of the master thesis: MSc. Benedikt Bergmann, Ph.D.

Study programme: Physics

Study branch: Particle and Nuclear Physics

Prague 2023

I declare that I carried out this master thesis independently, and only with the cited sources, literature and other professional sources. It has not been used to obtain another or the same degree.

I understand that my work relates to the rights and obligations under the Act No. 121/2000 Sb., the Copyright Act, as amended, in particular the fact that the Charles University has the right to conclude a license agreement on the use of this work as a school work pursuant to Section 60 subsection 1 of the Copyright Act.

In .... date ....
                                                 Author's signature

Title: Studies of the K-shell double vacancy production in the electron capture decays of ^{55}Fe, ^{54}Mn and ^{65}Zn using hybrid pixel detectors

Author: Bc. Martin Kaplan

Institute: Institute of Particle and Nuclear Physics

Supervisor: MSc. Benedikt Bergmann, Ph.D., IEAP, CTU in Prague

Abstract: The present thesis provides an experimental study of the K-shell double vacancy production in the electron capture decays of ^{55}Fe, ^{54}Mn, ^{65}Zn using a pair of Timepix3 detectors. Measured data are preprocessed and explored. The methodology for the calculation of the probability of K-shell double vacancy production in ^{55}Fe and ^{54}Mn is developed. Therefore, an extensive amount of signal and background processes were considered during the development of the methodology. The measurement setup is defined and optimized in the Allpix^2 framework for a simulation of detection efficiencies of particles participating in the signal and background processes. The probability of K-shell double vacancy creation in the electron capture decay of ^{55}Fe was measured to be $P_{\text{KK}} = (1.406 \pm 0.05) \times 10^{-4}$ with a systematic error of $\Delta_{\text{sys}}(P_{\text{KK}}) = {}^{+0.030}_{-0.034} \times 10^{-4}$. The value of P_{KK} for the electron capture decay of ^{54}Mn found to be $P_{\text{KK}} = (3.93 \pm 0.44) \times 10^{-4}$ with a systematic error of $\Delta_{\text{sys}}(P_{\text{KK}}) = {}^{+0.25}_{-1.11} \times 10^{-4}$. Resulting probabilities for K-shell double vacancy production in ^{55}Fe and ^{54}Mn are in agreement with the latest results.

Keywords: Electron capture decay Hybrid pixel detectors K-shell double vacancy production

Contents

Introduction

Electron capture decay is a process in which an inner shell electron interacts with a proton inside the nucleus. The interacting proton is transformed into a neutron and the Q-value of the decay is carried away by an electron neutrino. In the case of K-shell electron capture, there is a low probability in the region of $10^{-5} - 10^{-4}$ that the second K-shell electron is also affected due to electron-electron interactions and gets excited to a higher shell or most likely into the continuum. An atom with an empty K-shell is called a hollow atom [1]. Since the second K-shell would not be created without electron-electron interactions, studies of hollow atoms and their X-ray lines are an important probe into electron correlations within atoms [2]

The first experimental study of K-shell double vacancy production has been conducted by Charpak in 1953 by coincident detection of X-rays with a pair of proportional counters [3]. The value of P_{KK} has since then been measured several times with energy-sensitive detectors (NaI or Ge) usually being deployed in a coincidence setup [1]. The results of these measurements supported the tendency of P_{KK} to decrease with Z^{-2} [1] as predicted by the Primakoff-Porter theory [4]. The dependence of measured values of P_{KK} on Z is shown in Figure 1, where the Z^{-2} behavior is indicated.

A recent measurement was done in 2016 by Bergmann et al. with a pair of Timepix detectors [5], finding $P_{KK} = (1.388 \pm 0.037) \times 10^{-4}$ with a systematic error of $\Delta(P_{KK}) = 0.042 \times 10^{-4}$. The key shortcomings of this measurement setup have been the very long measurement time of approximately two years, due to a relatively high amount of dead time, and not having energy information. This is significantly improved by using a newer Timepix3 detector utilized within this thesis and featuring a (dead-time free) data-driven readout scheme and a simultaneous measurement of energy and time.

The double K-shell vacancy production in ^{54}Mn has been studied in 1984 by Nagy and Schupp [6] by measuring coincident X-rays of a ^{54}Cr atom produced in electron capture decay of ^{54}Mn. They measured the value of $P_{KK} = (3.6 \pm 0.3) \times 10^{-4}$. Another measurement has been done by Hindi in 2003 [7] with the measured value $P_{KK} = (2.3^{+0.8}_{-0.5}) \times 10^{-4}$. Nagy and Schupp also conducted a measurement of ^{65}Zn P_{KK} in 1983 with the result $P_{KK} = (2.2 \pm 0.2) \times 10^{-4}$ [8]. Values of P_{KK} predicted by various theories including Primakoff-Porter (PP) theory have been compared to measured values by Intemann in 1985 [9]. The presented table can be seen in Figure 2. A discrepancy between measured values (Expt.) and values predicted by Primakoff and Porter (PP) is apparent in ^{54}Mn and ^{65}Zn.

The double K-shell vacancy production in three distinct isotopes ^{55}Fe, ^{54}Mn and ^{65}Zn is studied in the experimental part of this thesis using a pair of Timepix3 hybrid pixel detectors. Measured data are first preprocessed and investigated. Methodology for calculation of P_{KK} in electron capture decay of ^{55}Fe and ^{54}Mn is developed and detection efficiencies of participating particles are simulated. Measured values of ^{55}Fe and ^{54}Mn P_{KK} are presented with an outlook on the calculation of ^{65}Zn P_{KK}.
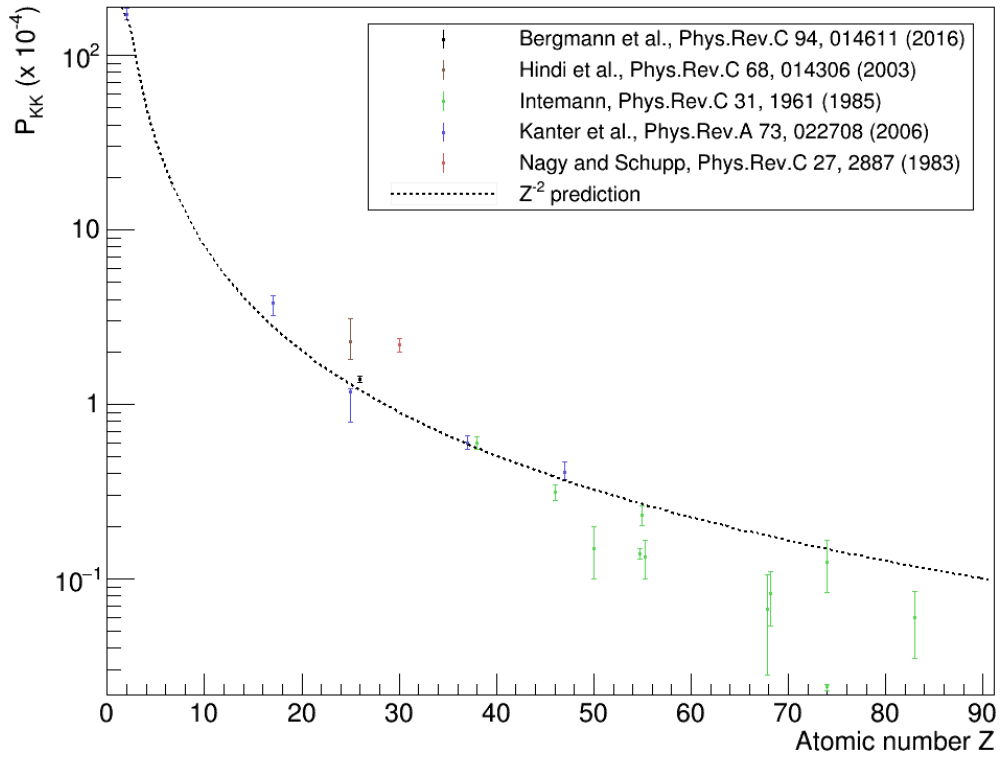
Figure 1: Overview of measured P_{KK} values as a function of the atomic number Z. The Z^{-2} predicted by Primakoff-Porter is indicated.

TABLE II. Comparison of various theories with recent experimental results.

Nuclide	$P_K(\times 10^{-5})$ Theory				Expt.	Ref.
	PP	MIKS	SRP	SL		
^{54}Mn	13.53		11.25	24.3	36 ±3	12
^{55}Fe	11.48	8.81	9.42	20.06	12 ±4	13
					10.1 ±2.7	14
^{65}Zn	8.65			15.3	22 ±2	15
^{71}Ge	6.92	4.56	5.08	11.84	12	16
^{85}Sr	5.27		3.38	9.38	6.0 ±0.5	17
^{103}Pd	3.27		1.74	6.03	3.13 ±0.31	18
^{109}Cd	0.63		0.34	0.89	15.2 ±2.4	19
					2.8 ±0.7	20
					1.02 ±0.36	21
^{113}Sn	2.79		1.34	5.33	1.5 ±0.5	22
^{131}Cs	1.76	0.71	0.75	3.22	1.33 ±0.33	23
					2.3 ±0.3	24
					1.4 ±0.1	25
^{165}Er	0.87	0.30	0.26	1.71	0.67 ±0.39	23
					0.82 ±0.28	26
^{181}W	0.076		0.022	0.14	0.24 ±0.06	26
					1.25 ±0.42	22
^{207}Bi	0.69		0.11[a]	1.97	0.6 ±0.25	27

[a]Contribution from 10% 2^+ branch not included.

Figure 2: Summary of theoretically predicted values of P_{KK} for various isotopes and a comparison to measured values. From [9]

1. Theoretical background

1.1 Double K-shell vacancy production during electron capture decay

Electron capture decay occurs when an electron from one of the shells interacts with the nucleus, reducing the proton number while increasing the neutron number each by 1. An electron neutrino can carry away energy up to the Q-value of the reaction. The whole process can be expressed subsequently:

$$^A_Z X + e^- \rightarrow\ ^A_{Z-1} Y + \nu_{e^-} \tag{1.1}$$

The vacancy left by the electron participating in the electron capture is then quickly filled by an electron from a higher shell, and an X-ray photon or an Auger electron is emitted. The two electrons residing in an atom's K-shell possess the highest probability to participate in this type of decay. The probability of K-shell electron capture is denoted P_K. There is a non-negligible probability for the second electron to be affected during K-shell electron capture and carry away part of the Q-value of the reaction. The second electron can either be elevated to a higher shell, also called the shake-up process, or it can travel away from the atom completely in the so-called shake-off process. In electron capture decay, the shake-off process is dominating, and the shake-off electron can carry away energy up to approximately the Q-value of the reaction. An atom with an empty K-shell is called a hollow atom, and both of the vacancies are almost instantly filled by electrons from higher shells. Either two x-rays or two Auger-electrons, or one of each, are emitted. In the case of two X-rays, the first one is called a hypersatellite photon, and the second one is called a satellite photon. The probability of X-ray emission due to a single K-shell vacancy is denoted ω_K and is also called fluorescence yield. In the case of K-shell double vacancy, fluorescence yields are denoted ω_{HS} and ω_S. Hypersatellite and satellite photons are characterized by slightly higher energies than corresponding main diagram lines due to a decrease in Coulomb shielding when spectator vacancies are present [10]. We denote the double K-shell vacancy production probability in electron capture decay as P_{KK}.

1.2 Decay of ^{55}Fe

^{55}Fe isotope decays solely by electron capture. The Q-value of the reaction is equal to 231.31 keV. The half-life of the isotope is 2.747 years. As can be seen in Figure 1.1, there is a negligible probability of the isotope decaying into an excited state of ^{55}Mn which subsequently decays by gamma emission. This happens only in $1.3 \times 10^{-7}\%$ of all electron capture decays of ^{55}Fe.

K-shell electron capture is accompanied either by K-line X-ray photon or by Auger electron from produced a ^{55}Mn atom. The energy of K-line X-ray photons can be found in Table 1.1. Fluorescence yield in the case of K-line X-ray photons is $\omega_K = (0.321 \pm 0.007)$ [11].

There is a probability of $P_{IB} = (2.58 \pm 0.04) \times 10^{-5}$ [12] for ^{55}Fe electron capture decay to be accompanied by internal bremsstrahlung (IB) photon, which
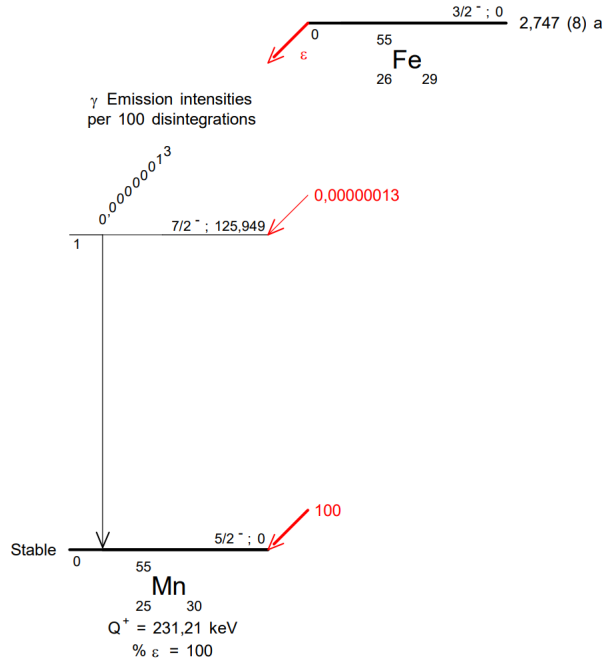
Figure 1.1: Scheme of nuclear decay of ^{55}Fe [11].

Line	Energy [keV]	Relative prob.
$K\alpha_2$	5.88765	51
$K\alpha_1$	5.89875	100
$K\beta_3$	6.49045	20.5
$K\beta_5''$	6.5352	20.5

Table 1.1: Energies of K-line X-ray photons following electron capture decay of ^{55}Fe [11].
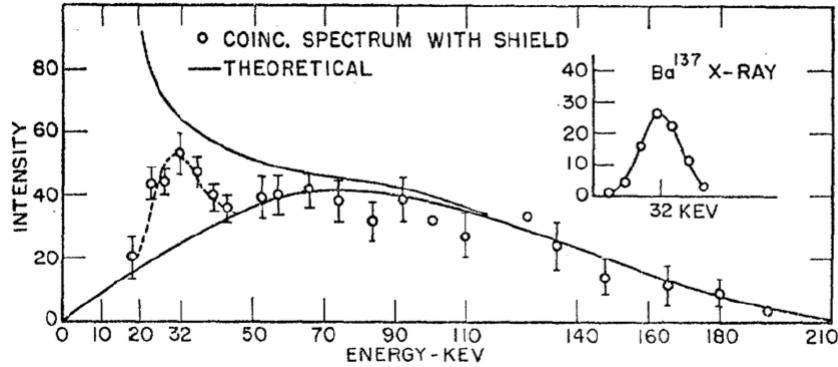
Figure 1.2: The energy spectrum of coincident bremsstrahlung emitted in electron capture decay of ^{55}Fe. Solid curves correspond to theoretical predictions shown for comparison with the measured values [14].

can be emitted with energy up to the Q-value of the reaction. Spectrum of ^{55}Fe internal bremsstrahlung is shown in Figure 1.2. There is also a chance that electron capture is accompanied by a shake-off electron. The probability for K-shell and L-shell shake-off electrons can be found in [13], and we denote the joint probability as P_{KLLK}. The spectrum of shake-off electrons can be seen in Figure 1.3.

1.3 Decay of ^{54}Mn

^{54}Mn decays mostly by electron capture with a negligible branching ratio for β^+ decay. The half-life of the isotope is 312.19 days. In almost all of the cases, ^{54}Mn decays into an excited level of ^{54}Cr which consequently decays by γ-ray emission of approximately 835 keV to the ground state of ^{54}Cr. The scheme of the decay is shown in Figure 1.4.

The decay can be accompanied by a shake-off electron and by an IB photon with probability $P_{\mathrm{IB}} = (6.5 \pm 1.5) \times 10^{-5}$ [17]. The spectrum of IB photons is shown in Figure 1.5.

Since ^{54}Mn decays almost always to an excited state of daughter nucleus, aside from γ-ray emission, it may also deexcite by internal conversion (IC). During such a process, the excited nucleus electromagnetically interacts with an atomic electron, which is then released with energy close to the γ-ray. Internal conversion involving the second K-shell electron creates a second vacancy in the K-shell. It thus acts as a competing process to K-shell double vacancy creation in electron capture decay. The probability of internal conversion in case of an excited daughter nucleus following electron capture decay of ^{54}Mn is called an internal conversion coefficient $\alpha_{\mathrm{T}} = (2.45 \pm 0.04) \times 10^{-4}$ [16]. We denote the internal conversion coefficients for separate shells as α_{K}, α_{L} and α_{M}.

K-shell electron capture decay may be accompanied by a K-line X-ray photon with fluorescence yield $\omega_{\mathrm{K}} = (0.289 \pm 0.005)$ [16], their energies can be found in Table 1.1.
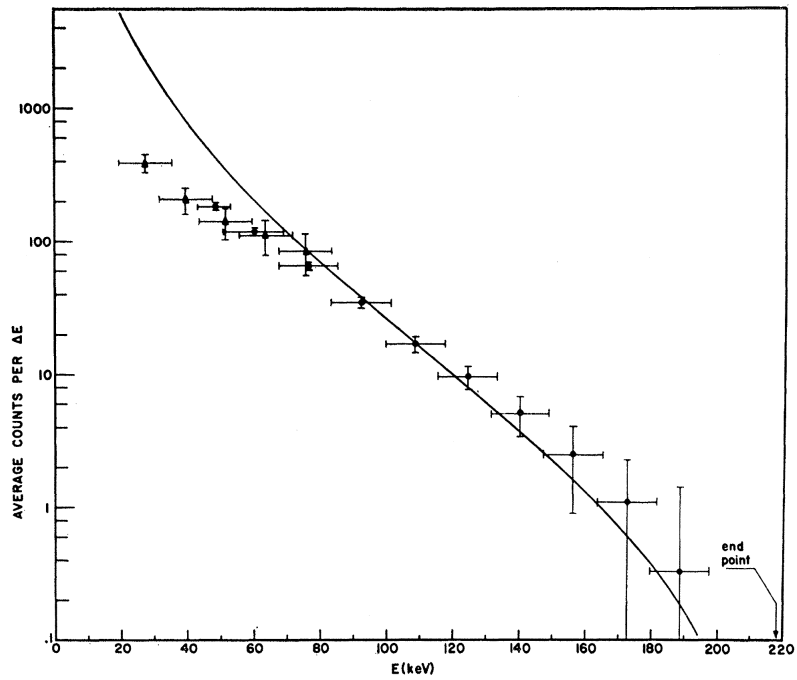
Figure 1.3: The energy spectrum of shake-off electrons emitted in electron capture decay of ^{55}Fe. The solid curve corresponds to a theoretical spectrum shown for comparison with the measured values [15].
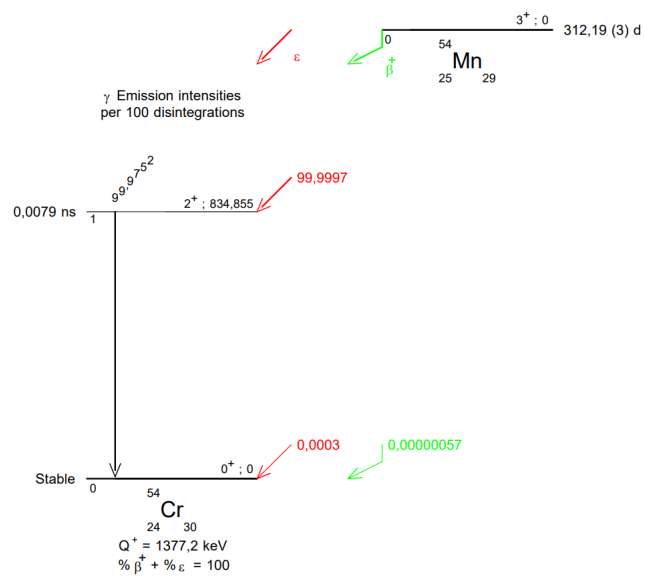

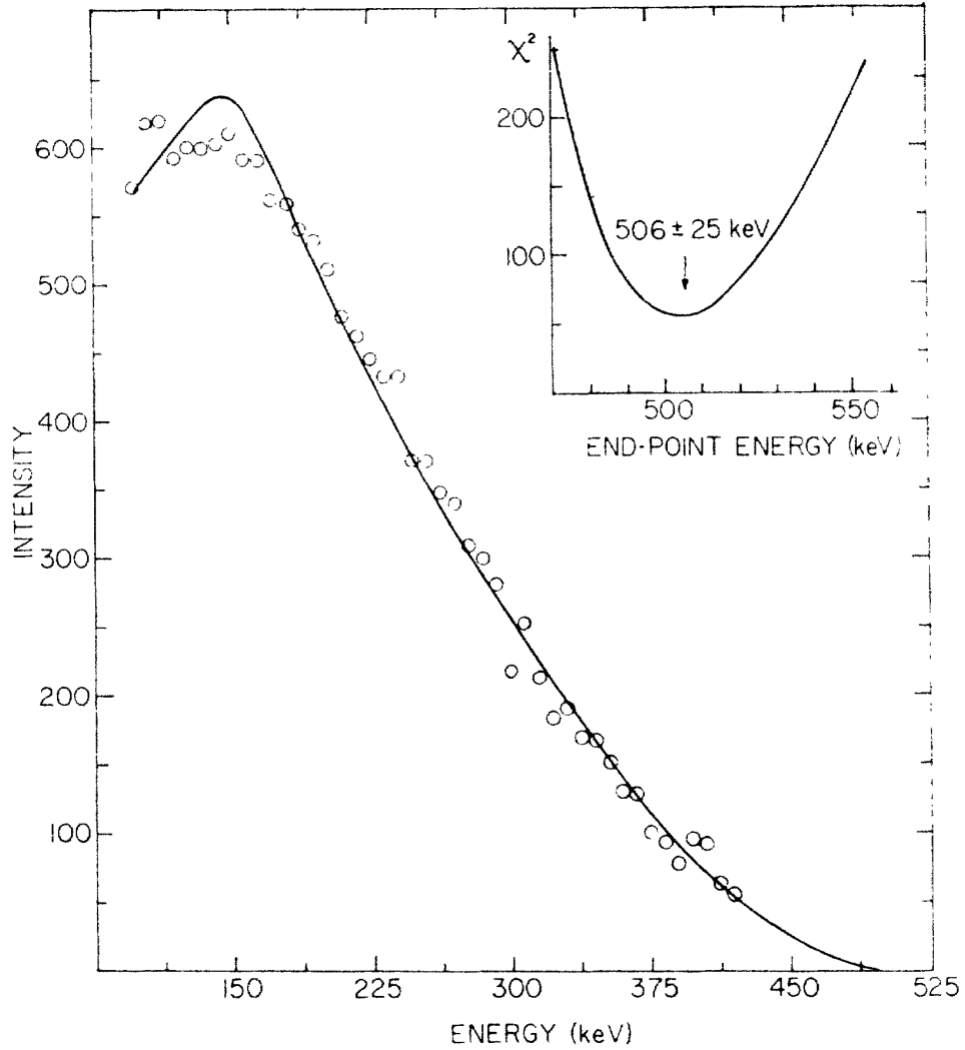Figure 1.4: A scheme of nuclear decay of ^{54}Mn [16].

7

Figure 1.5: The energy spectrum of internal bremsstrahlung emitted in electron capture decay of ^{54}Mn. [17].

Line	Energy [keV]	Relative prob.
$K\alpha_2$	5.40557	50.91
$K\alpha_1$	5.41479	100
$K\beta_1$	5.94667	20.31
$K\beta_5''$	5.987	20.31

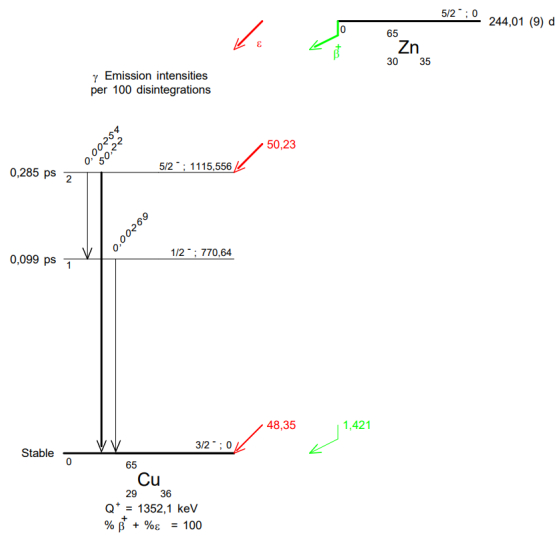Table 1.2: Energies of K-line X-ray photons following electron capture decay of ^{54}Mn [16].

8

γ Emission intensities
per 100 disintegrations

5/2⁻ ; 0 244,01 (9) d

Figure 1.6: Scheme of the nuclear decay of ^{65}Zn [18].

Line	Energy [keV]	Relative prob.
$K\alpha_2$	8.02792	51.33
$K\alpha_1$	8.04787	100
$K\beta_1$	8.90539	21.05
$K\beta_5''$	8.9771	21.05

Table 1.3: Energies of K-line X-ray photons following electron capture decay of ^{54}Mn [18].

1.4   Decay of ^{65}Zn

^{65}Zn isotope decays either by β^+ with branching ratio of 1.421 and by electron capture. By the latter, it decays either to an excited level of ^{65}Cu with a branching ratio of 50.23 or to a ground level with a branching ratio of 48.35. The excited level then almost immediately decays by γ emission either to another excited level and then to the ground level or directly to the ground level. ^{65}Zn decays with a half-life of 244.01 days and the scheme of the decay is shown in Figure 1.6

Same way as for the previous two isotopes, electron capture decay of ^{65}Zn may be accompanied by shake-off electron, IB photon, γray photon, or by IC electron. K-shell electron capture decay is accompanied either by an Auger electron or by K-line X-ray photon; their energies can be found in Table 1.3 and the fluorescence yield is $\omega_{\mathrm{K}} = (0.454 \pm 0.004)$.

2. Experimental setup and methods

2.1 Timepix3

The Timepix3 detector is a hybrid pixel detector designed and developed within the Medipix3 collaboration [19]. The fundamental idea behind hybrid pixel detectors is the separation of the detection medium, which is commonly referred to as the sensor layer, from the readout electronics. This allows the user to choose the material for the sensor layer according to the application. The most commonly used materials include semiconductors like silicon, GaAs, and CdTe. Flip-chip bump-bonding (also called solder bonding) [20] is used to connect each pixel of the sensor layer to the electronics in the readout chip, as can be seen in Figure 2.1 illustrating assembly of the detector [1]. Katherine readout [21] has been used for the measurement of data analyzed in this thesis.

2.1.1 Working principle

The working principle of Timepix3 detectors can be explained as follows. The sensor layer is fully depleted by an applied reverse bias voltage. Incoming ionizing radiation creates free charge carriers in the sensor layer, negatively charged electrons, and positively charged holes, with their number being proportional to the deposited energy. The produced electrons and holes then drift through the sensor layer either to the pixelated side or the common electrode. The direction depends on their charge. In our case, electrons drift toward the backside, holes towards the pixelated electrode. During this process, electric currents are induced at the nearest pixels and subsequently converted to voltage pulses, which are shaped and amplified by the analog part of the electronics present in each pixel. The voltage pulses are then compared to an adjustable threshold level (THL), as shown in Figure 2.2. The time of arrival of a particle is measured by the pulse crossing of THL on the rising edge, and the deposited energy is measured by the time, during which the pulse remains over THL, or so-called Time-over-Threshold (ToT). Deposited energy is proportional to ToT. To calculate deposited energy from the measured ToT, the detector needs to be calibrated, meaning we need to know the $E(ToT)$ dependency for each pixel. We can obtain this by calibration with characteristic X-ray fluorescence lines [22].

Timepix3 features a data-driven readout scheme capable of measuring time of arrival (ToA) and time over threshold (ToT) independently in each pixel. The pixelated side is divided into $256 \times 256 = 65{,}536$ pixels, and a time resolution of 1.5625 ns can be achieved. Noise-free operation of Timepix3 should be possible at THL = 500 e$^-$, which is equal to 1.8 keV in silicon [1]. Tracks of particles measured by the Timepix3 detector are called clusters. An example of clusters can be seen in Figure 2.3.
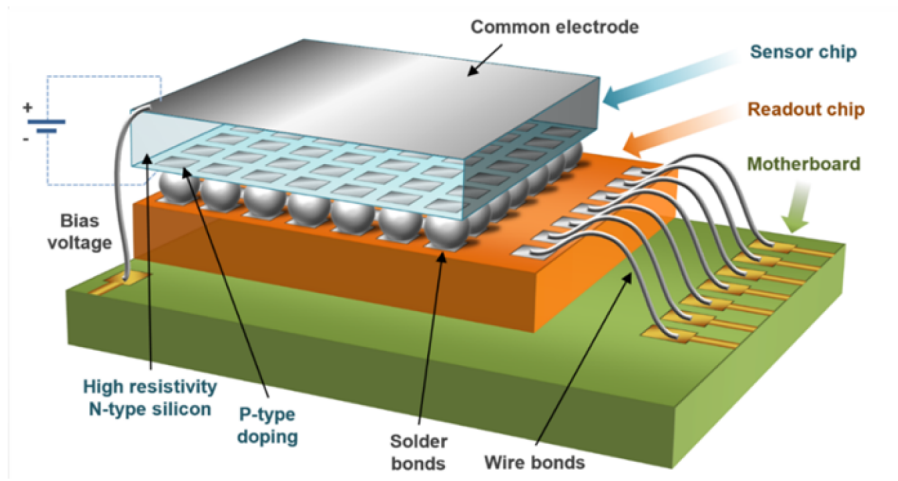
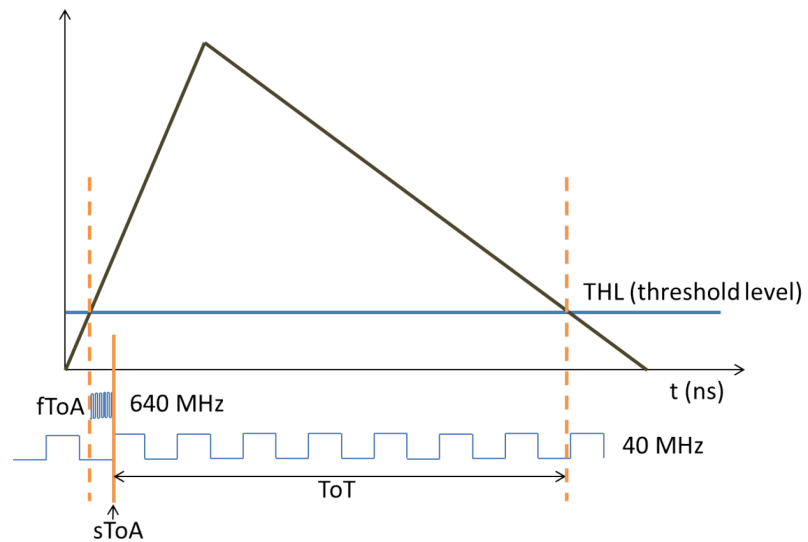Figure 2.1: An illustration of the Timepix3 detector in assembly [1].

.

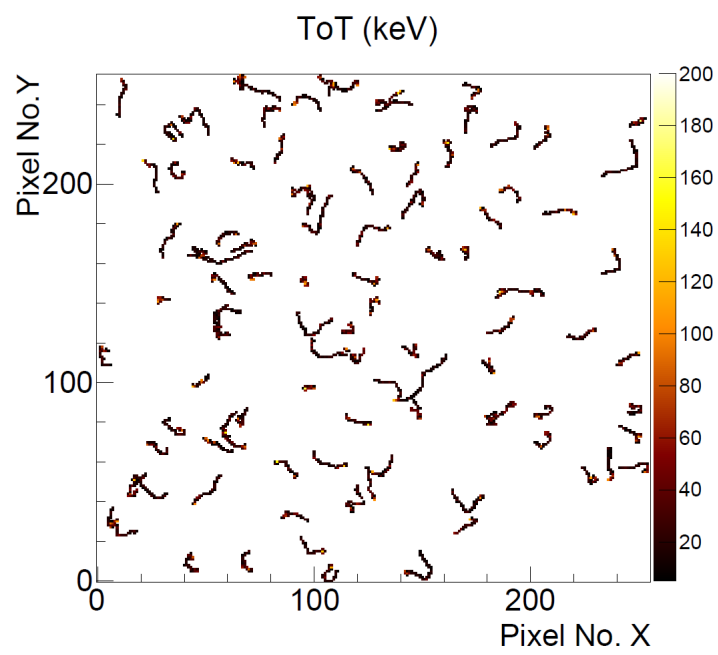Figure 2.2: An illustration of working principles of the Timepix3 detector [1].

Figure 2.3: Electrons from internal conversion and from the photoelectric effect of 835 keV photons from decay of ^{54}Mn measured by the Timepix3 detector [1].
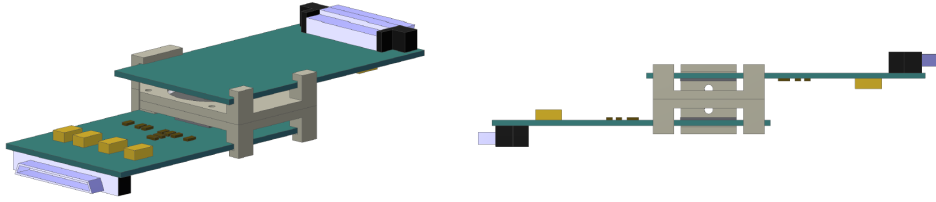
Figure 2.4: A scheme of the measurement setup showing a pair of Timepix3 detector facing each other [2]. The sensor parts can be found in the center where the detectors are held by the holder. The radiation source can be found in between the sensors.

2.2 Experimental setup

All measured data used throughout this thesis have been measured in Erlangen Centre for Astroparticle Physics (ECAP) in Germany. A pair of Timepix3 detectors with 500 μm thick silicon sensor has been used with sensors facing each other with a radioactive source placed in the middle. The sources are small drops of radioactive material enveloped in polyethylene foil. A scheme of the measurement setup is shown in Figure 2.4.

2.3 Software

Several software tools have been used in the experimental part of the thesis. The most important one has been the ROOT framework [23], which is a powerful tool for data processing developed at CERN and is widely used for data analysis in particle and nuclear physics. ROOT can be used either interactively, within a fully compiled C++ program, or by utilizing a set of prepared bindings to use in Python scripts. All these approaches have been used throughout the experimental work.

Clustering software developed by scientists at IEAP used to reconstruct tracks from simulated or measured data has been utilized throughout the experimental part of this thesis. The idea of clustering is that we group pixels hits that are time ($\Delta t < 200$ ns) and spatially (8-fold neighborhood) coincident. Such groups of pixel hits are then called clusters. Their attributes are calculated and stored in ROOT files.

Allpix^2 is a simulation framework for semiconductor particle detectors developed in C++ [24]. It utilizes the well-known Geant4 framework for the deposition of charge carriers while the core of the Allpix^2 framework focuses on the simulation of charge carriers transport in semiconductor detectors. The reconstruction of tracks has to be performed by the user [25]. The framework is configured by the use of configuration files, three of which are mandatory [26]:

- **Main configuration file** - the most important one, it includes a global framework definition and the list of modules with their configuration to be executed in the given order. An example of the main configuration file used within the experimental part of this thesis:

```
[AllPix]
log_level = "WARNING"
log_format = "DEFAULT"
detectors_file = "Si_geometry_twin.conf"
model_paths = "/simulations/Mn_54/K_lines/models"
output_directory = "/simulations/Mn_54/K_lines/output/"
root_file = "modules.root"
number_of_events = 5000000

[GeometryBuilderGeant4]
world_material = "air"

[DepositionGeant4]
physics_list = FTFP_BERT_LIV
source_type = "macro"
file_name = "/simulations/Mn_54/K_lines/source.g4mac"
max_step_length = 1um
range_cut = 200um

[ElectricFieldReader]
model = "linear"
bias_voltage = 230V
depletion_voltage = 80V
output_plots = true

[GenericPropagation]
temperature = 315K
charge_per_step = 20
integration_time = 40ns
propagate_holes = true
propagate_electrons = false
output_plots = true

[PulseTransfer]
timestep = 0.1ns

[ROOTObjectWriter]
exclude = PropagatedCharge
file_name = "data_out.root"
```

- **Geometry configuration file** - a file used for the configuration of the detector positions and passive materials. An example of a geometry configuration file used within the experimental part of this thesis:

```
[detector0]
type = "timepix"
position = 0.193mm −0.065mm 5.05mm
orientation_mode = "zyx"
orientation = 0deg 0deg 0deg

[detector1]
type = "timepix"
position = 0.020mm 0.135mm −4.95mm
orientation_mode = "zyx"
orientation = 180deg 180deg 0deg

[cylinder1]
type = "cylinder"
outer_radius = 15mm
inner_radius = 0mm
length = 0.052mm
position = 0mm 0mm 0mm
orientation = 0 0deg 0deg
material = "polyethylene"
role = "passive"
```

- **Detector model configuration file** - a file containing parameters of the detector model used in the simulation. An example of a detector model configuration file containing the definition of the Timepix3 detector:

```
type = "hybrid"

number_of_pixels = 256 256
pixel_size = 55um 55um

sensor_thickness = 500um
sensor_excess = 1mm

bump_sphere_radius = 9.0um
bump_cylinder_radius = 7.0um
bump_height = 20.0um

chip_thickness = 300um
chip_excess_left = 15um
chip_excess_right = 15um
chip_excess_bottom = 2040um

[support]
thickness = 1.76mm
size = 47mm 79mm
offset = 0 -22.25mm

[support]
thickness = 1.0um
size = 14mm 14mm
material = "silicon"
location = "absolute"
offset = 0um 0um -500.5um

[support]
thickness = 0.8um
size = 14mm 14mm
material = "aluminum"
location = "absolute"
offset = 0um 0um -501.4um
```

3. Experimental studies of double K-shell vacancy production in electron capture decay

Data for the experimental studies performed in this thesis has been acquired at ECAP by performing measurements with the double-sided stack of Timepix3 detectors explained in Section 2.2. The measurement software saves measured data to files with a specific structure containing information about the detector's settings applied during the measurement and information about pixel hits, namely the position, ToA, and ToT. To analyze measured data correctly, we need to process them using Clustering software. The output of this process is a ROOT file containing two ROOT trees with information about both detectors settings and a tree with clustered data (one entry per cluster). The most important cluster quantities contained in the ROOT files are cluster energy, cluster size, time of arrival, layer number etc. The energy of a cluster is obtained by summing individual energies in pixels belonging to the cluster. Cluster size is the number of pixels forming a cluster. Time of arrival is given by the lowest ToA in individual pixels in the cluster. Layer number indicates in which detector the cluster was detected, and in the case of our experiment, it can only have a value of 1 or 2.

3.1   Data preprocessing

Several effects need to be considered during data preprocessing. ToA values need to be corrected for the time-walk effect, a time offset between the two detectors, noisy pixels need to be identified and masked, and a ToA bug in several columns of pixels needs to be adjusted for. The time-walk effect is caused by the dependence of the slope of the rising signal on the pulse height. This causes a dependency of the measured timestamp on the pulse height and is corrected in the data preprocessing [27]. Noisy pixels were masked manually by spotting them in a 2D histogram of pixel hits. The mask is then understood to be a text file with a (256, 256) matrix full of values 1 or 0. Value 1 means the pixel is masked, while value 0 means the pixel is not masked. Masks of noisy pixels are then utilized in subsequent analysis in which clusters hitting masked pixels are considered as noise and are removed from the analysis. A measured 2D histogram of pixel hits with noisy pixels masked can be found in Figure 3.1.

The ToA bug in several columns of pixels is visible in Figure 3.2. During the preprocessing of measured data, it became apparent that this bug only occurs in the interval of columns (170:210) where measured ToA in some columns of pixels gets shifted by 25 ns. The approach chosen to correct this bug was to write a Python script that plots average ΔToA in columns of pixels, locates columns suffering from the bug, and produces text files indicating which columns need to be shifted by ± 25 ns during Clustering. Histograms in Figure 3.3 show the effect of these corrections on the histogram of ΔToA normalized by pixel hits. With this approach, every measurement file has received a specific correction file for this type of bug.
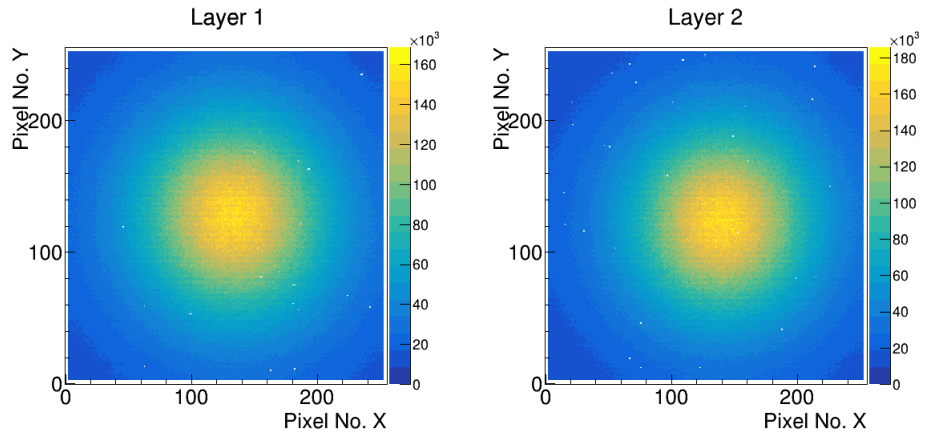
Figure 3.1: The histogram of pixel hits measured with ^{55}Fe source and with noisy pixels masked.
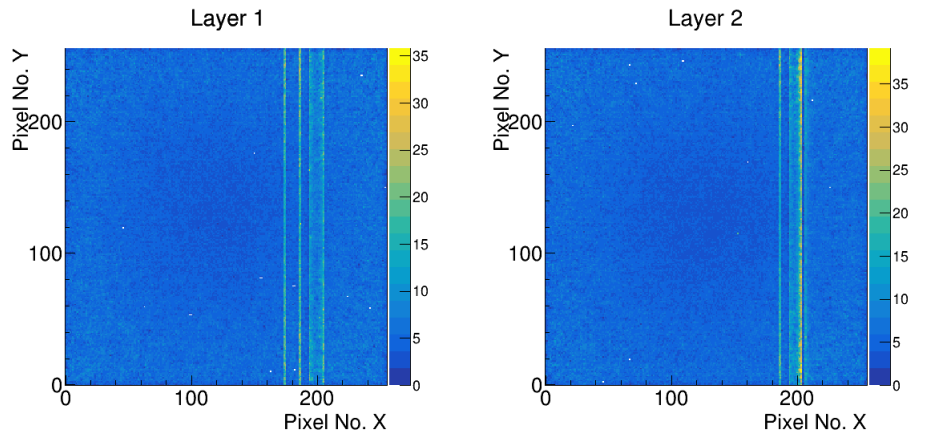

Figure 3.2: The histogram of ΔToA divided by histogram of hits in a dataset measured with ^{54}Mn source displaying the ΔToA bug.
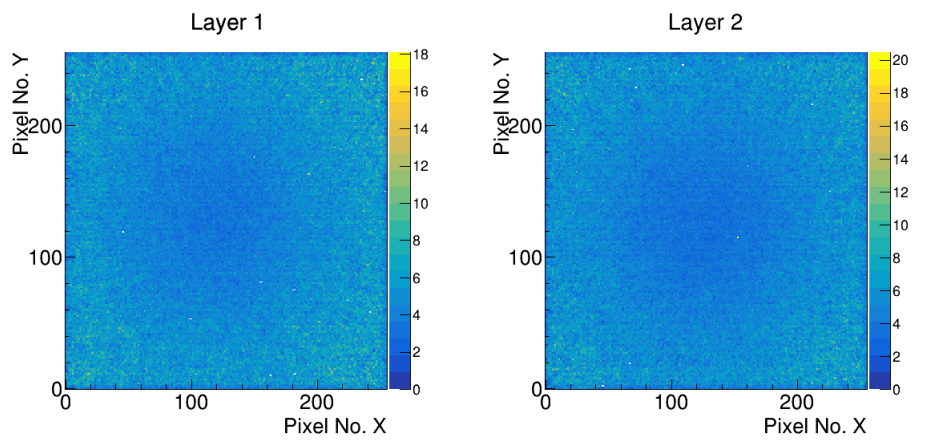

Figure 3.3: The histogram of ΔToA divide by histogram of hits in a dataset measured with ^{54}Mn source with the ΔToA bug corrected.
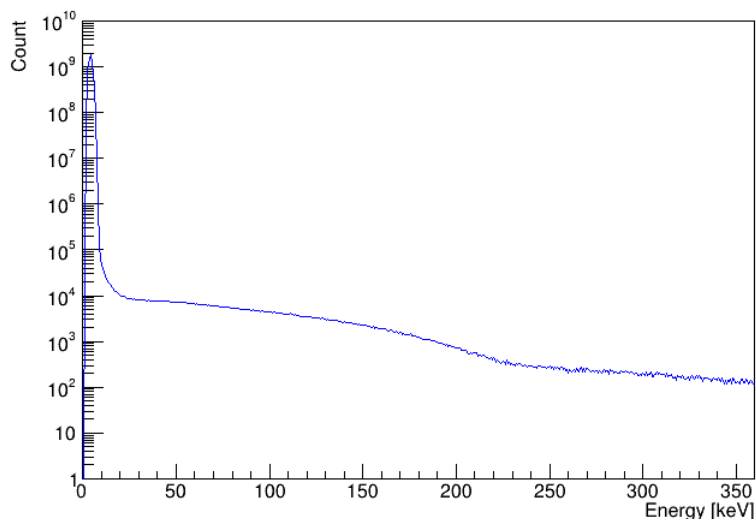
Figure 3.4: The measured energy spectrum of ^{55}Fe. The peak at energy < 20 keV is dominated by K-line X-ray photons emitted after K-shell electron capture decay. The end-point of the IB photons spectrum and the shake-off electrons spectrum is expected at 231 keV and visible.

3.2 Measurement with ^{55}Fe source

Measurement has been conducted using a ^{55}Fe radioactive source. The manufacturer has supplied information on the activity of the source, and it was $A_0 = (195 \pm 3)$ kBq on January 1, 2013, 00:00. Measurement with the source using the setup explained in Section 2.2 has been performed with a total of 13.5 days of measurement time. The energy spectrum of measured clusters is shown in Figure 3.4.

Thanks to the knowledge of the activity of the source, we can calculate the activity of the source during the measurement, and from the measured number of clusters in an energy region of [3, 13] keV, we can calculate detection efficiency δ_{K} of the setup for K-line X-ray photons of the ^{55}Mn atom to which ^{55}Fe decays by electron capture. Detection efficiency is defined as:

$$\delta_{\mathrm{K}} = \frac{N_{\mathrm{meas}}}{N_{\mathrm{emit}}} = \frac{N_{\mathrm{meas}}}{A(t)\, t\, P_{\mathrm{K}}\, \omega_{\mathrm{K}}} \tag{3.1}$$

where

$$A(t) = A_0\, exp\left(\frac{-ln(2)}{T_{1/2}} t_{\mathrm{meas}}\right) \tag{3.2}$$

and where N_{meas} is a number of measured clusters in the energy region of [3, 13] keV, N_{emit} is a number of K-line X-ray photons emitted after electron capture decay, t stands for measurement time, P_{K} is the probability of K-shell electron capture decay, ω_{K} is the corresponding fluorescence yield. Values used for calculation and the resulting δ_{K} are shown in Table 3.1

The value of δ_{K} for the setup stands at $\delta_{\mathrm{K}} = (0.384 \pm 0.001)$ with the systematic error $\Delta_{syst}(\delta_{\mathrm{K}}) = 0.006$ which was determined from the error of the activity

Quantity	Value	$\sigma(x)$	$\Delta_{syst}(x)$	Source
A [kBq]	53.9		0.8	measured
t [s]	1164760			measured
t [d]	13.5			measured
N_{meas}	6832441643	82659		measured
P_{K}	0.8853		0.0016	[11]
ω_{K}	0.321		0.007	[11]
δ_{K}	0.384	0.001	0.006	measured

Table 3.1: Quantities used for calculation of δ_{K}.

of the source supplied by the manufacturer. The radioactive source's activity A was assumed to be constant for the calculation and a value in the middle of the measurement time was chosen. The calculated value of δ_{K} was then used to calculate and plot the source's activity throughout the measurement. The result is shown in Figure 3.5.

The ultimate goal of the measurement with ^{55}Fe source is the measurement of P_{KK}. To do that, we utilize Timepix3's time resolution and measure incoming pairs of particles in coincidence. The time spectrum of two coincident clusters is shown in Figure 3.6

The peak of true coincidences is clearly visible in the time spectrum in the region of $\Delta\mathrm{ToA} < 40$ ns. By fitting a constant to the region of random coincidences, we can estimate their contribution to the region of true coincidences. We locate the endpoint of the region of true coincidences as the first bin of the histogram, in which the value is lower than the constant fit to the region of random coincidences $C = (39955\pm17)$. This way, we calculate the contribution of random coincidences to the region of true coincidences as $N_{\mathrm{acc}} = (1718602\pm1366)$. The total number of coincidences in the true coincidences region is equal to $N_{\mathrm{peak}} = (1867184\pm1311)$. The number of true coincidences is then equal then calculated as:

$$N_{\mathrm{true}} = N_{\mathrm{peak}} - N_{\mathrm{acc}}$$

and is equal to $N_{\mathrm{true}} = (148582 \pm 2677)$. We will utilize the number of true coincidences in the calculation of P_{KK}.
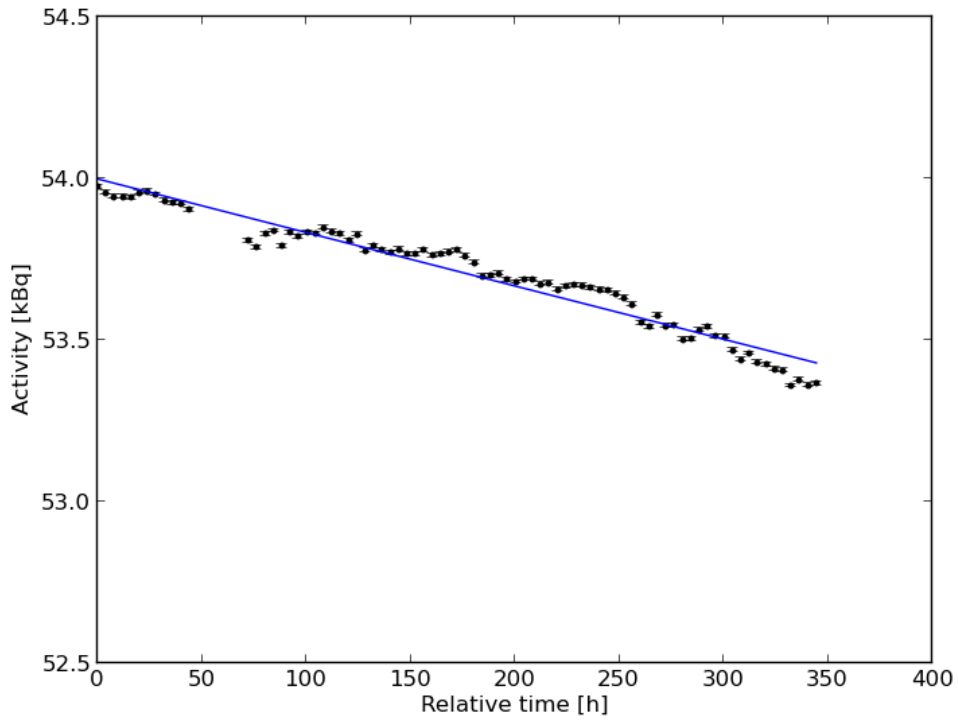
Figure 3.5: A measurement of the ^{55}Fe source activity with Timepix3 detectors. We fit an exponential $exp(ax + b)$ to the data with resulting coefficients: $a = (-3.08 \pm 0.27) \times 10^{-5}$, $b = (3.99 \pm 0.19)$.
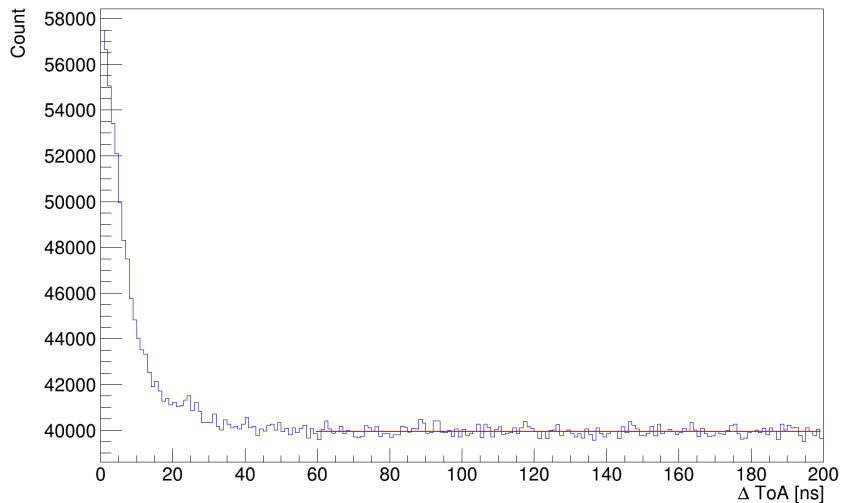

Figure 3.6: The time spectrum of two coincident clusters from ^{55}Fe. The spectrum was fitted by a constant in the flat region, with result $C = (39955 \pm 17)$, to estimate the number of random coincidences in the region of true coincidences ($\Delta\text{ToA} < 40$ ns). Only clusters of energy [3,13] keV are considered.

21

3.2.1 Derivation of methodology for calculation of ^{55}Fe P_{KK}

Processes contributing to signal

In the calculation of the P_{KK} for ^{55}Fe, we have to consider the main processes contributing to the measured signal in the two-particle coincidences measurement. The first process considered is the K-shell electron capture, in which the second K-shell electron is emitted from the atom due to electron-electron interaction. Hypersatellite and satellite photons are subsequently emitted. Three particles in total are emitted and can be detected. This gives three distinct contributions in two particles coincidence measurement:

$$N_{HS,S} = \frac{N_K}{\delta_K \omega_K} P_{KK} \, \delta_{HS} \, \delta_S \, \omega_{HS} \, \omega_S \, (1 - \delta_e) = P_{KK} N_{HS,S}^* \tag{3.3}$$

$$N_{HS,e} = \frac{N_K}{\delta_K \omega_K} P_{KK} \, \delta_{HS} \, (1 - \delta_S) \, \omega_{HS} \, \omega_S \, \delta_e = P_{KK} N_{HS,e}^* \tag{3.4}$$

$$N_{S,e} = \frac{N_K}{\delta_K \omega_K} P_{KK} \, (1 - \delta_{HS}) \, \delta_S \, \omega_{HS} \, \omega_S \, \delta_e = P_{KK} N_{S,e}^* \tag{3.5}$$

while using the relation $A(t) t_{meas} = \frac{N_K}{P_K \omega_K \delta_K}$. The letters in the subscript of N indicate the particles detected. The second set of contributions comes from the same process, the only difference being that instead of either a hypersatellite or satellite photon, an Auger electron is emitted. Their low energy means they will not reach the sensor and cannot be detected. Due to this fact, we get only two contributions from such a process:

$$N_{HS,e}^{SAuger} = \frac{N_K}{\delta_K \omega_K} P_{KK} \, \delta_{HS} \, \omega_{HS} \, (1 - \omega_S) \, \delta_e = P_{KK} N_{HS,e}^{*SAuger} \tag{3.6}$$

$$N_{S,e}^{HSAuger} = \frac{N_K}{\delta_K \omega_K} P_{KK} \, \delta_S \, (1 - \omega_{HS}) \, \omega_S \, \delta_e = P_{KK} N_{S,e}^{*HSAuger} \tag{3.7}$$

We will denote the sum of all five combinations of δ_S, δ_{HS}, δ_e, ω_S, ω_{HS} as Δ_{KK}.

Processes contributing to background

We have to also consider major background processes. The first is the coincident detection of two K-line X-rays from two separate K-shell electron captures. The contribution of this process can be estimated by fitting a straight line to the linear part of the time spectrum and is denoted as N_{acc}. The second background process considered is a coincident detection of K-line X-ray from K-shell electron capture and an internal bremsstrahlung photon:

$$N_{K,IB} = N_K \, P_{IB} \, \delta_{IB} \tag{3.8}$$

The last background process considered involves K-capture and L-shake-off or L-capture and L-shake-off. In both cases, we can only detect the K-line X-ray and the shake-off electron as the L-line X-ray has too low energy to be detected (0.5 - 0.6 keV [11]). The contribution of this process amounts to the following:

$$N_{K,e} = N_K P_{KLLK} \delta_e \tag{3.9}$$

Final formula for P_{KK}

The final formula for calculation of P_{KK} can then be derived subsequently:

$$
\begin{aligned}
N_{\text{peak}} &= P_{\text{KK}}(N^*_{\text{HS,S}} + N^*_{\text{HS,e}} + N^*_{\text{S,e}}N^{*\text{SAuger}}_{\text{HS,e}} + N^{*\text{HSAuger}}_{\text{S,e}}) + N_{\text{acc}} + N_{\text{K,IB}} + N_{\text{K,e}} \\
P_{\text{KK}} &= \frac{N_{\text{true}} - N_{\text{K,IB}} - N_{\text{K,e}}}{N^*_{\text{HS,S}} + N^*_{\text{HS,e}} + N^*_{\text{S,e}} + N^{*\text{SAuger}}_{\text{HS,e}} + N^{*\text{HSAuger}}_{\text{S,e}}}
\end{aligned}
$$

The formula can be written as follows:

$$
P_{\text{KK}} = \frac{\delta_{\text{K}}\,\omega_{\text{K}}}{\Delta_{\text{KK}}}\left(\frac{N_{\text{true}}}{N_{\text{K}}} - P_{\text{IB}}\delta_{\text{IB}} - P_{\text{KLLK}}\delta_{\text{e}}\right) \tag{3.10}
$$

23
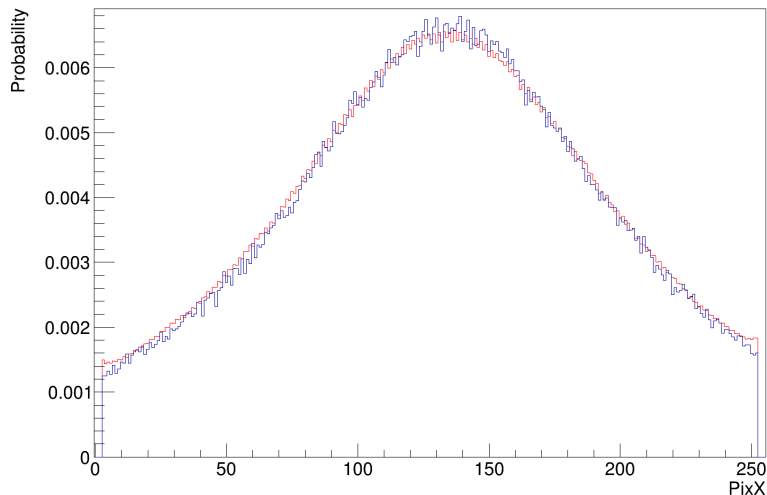
Figure 3.7: Comparison of measured and simulated pixel hits data. Projection to the X axis in layer 1. The blue line corresponds to the simulated data, while red to the measured data.

3.2.2 Optimization of setup in the simulation framework

To be able to simulate all the detection efficiencies, we need to first establish the correct geometry of the measurement setup inside the simulation framework. We use the K-line photons signal to optimize the geometry of the measurement setup within the Allpix^2 simulation framework. During this process, the size of the radioactive source, the thickness of the PE foil in which the source is wrapped, and the distance to both detectors were varied within the framework to achieve similar δ_K as during measurement while maintaining a similar structure of pixel hits as shown in Figure 3.1. This comparison was made by plotting simulated and measured projections of pixel hits to the X and Y axis; results can be seen in Figures 3.7 - 3.10.

To remind ourselves, δ_K of the measurement setup was calculated to be $\delta_K = (0.384 \pm 0.001)$. After optimization of the simulation setup, a value of $\delta_K^{sim} = (0.383 \pm 0.001)$ was achieved with the energy of K-line X-ray photons set at 6.03 keV as a properly weighted average value taken from [11].

Following detection efficiencies were simulated using the optimized setup:

- δ_S - detection efficiency for satellite photons. their energy was set at 6.09 keV [10]

- δ_{HS} - detection efficiency for hypersatellite photons. their energy was set at 6.3 keV [28]

- δ_e - detection efficiency for shake-off electrons, their energy was set as a spectrum taken from [15]

- δ_{IB} - detection efficiency for internal bremsstrahlung photons, their energy was set as a spectrum taken from [14]

The resulting values of simulated detection efficiencies are summarized in Table 3.2 in the following section.
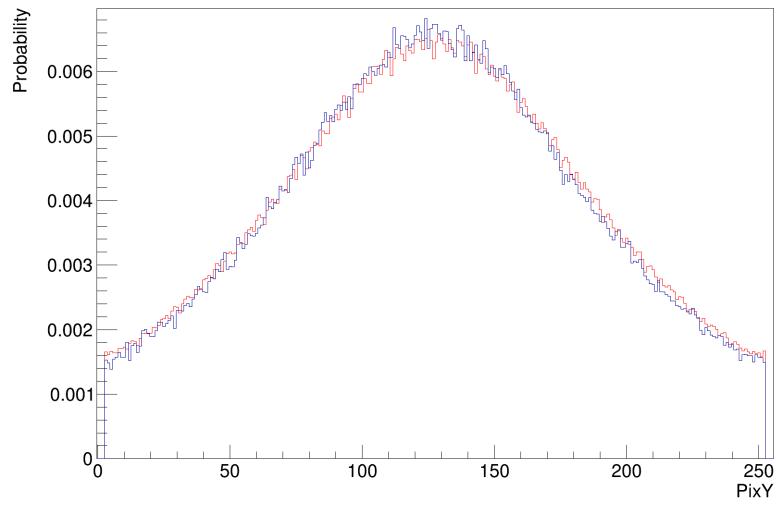
Figure 3.8: Comparison of measured and simulated pixel hits data. Projection to the Y axis in layer 1. The blue line corresponds to the simulated data, while the red to the measured data.
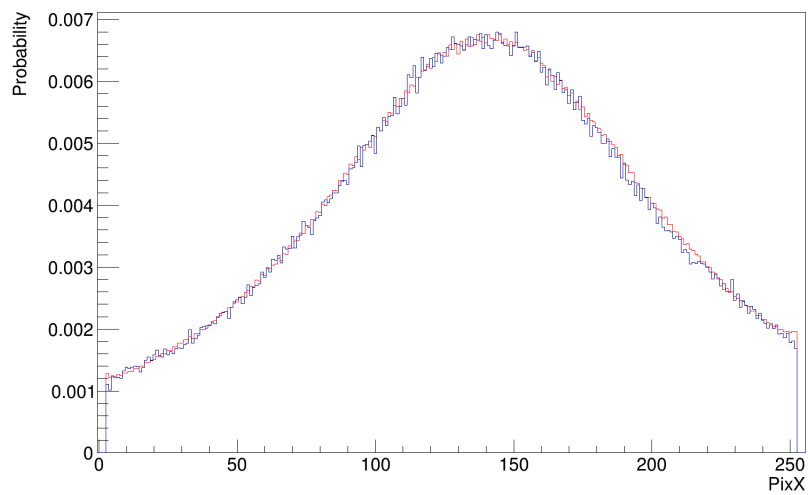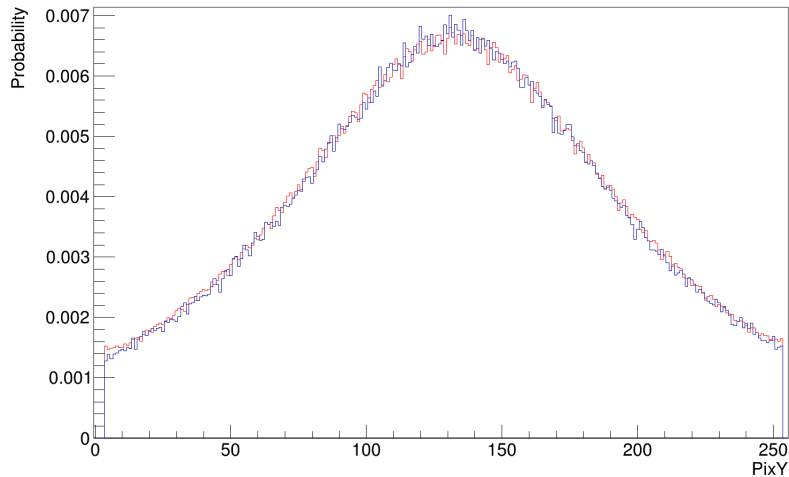

Figure 3.9: Comparison of measured and simulated pixel hits data. Projection to the X axis in layer 2. The blue line corresponds to the simulated data, while the red to the measured data.

Figure 3.10: Comparison of measured and simulated pixel hits data. Projection to the Y axis in layer 2. The blue line corresponds to the simulated data, while the red to the measured data.

3.2.3 Calculation of P_{KK}

All the values needed for the calculation of P_{KK} can be found in Table 3.2.

We can calculate signal and background contributions, results of these calculations can be found in the following Tables 3.3 and 3.4.

The P_{KK} value for ^{55}Fe amounts to:

$$P_{KK} = (1.406 \pm 0.005) \times 10^{-4}$$

with systematic error of $\Delta_{sys}(P_{KK}) = {}^{+0.030}_{-0.034} \times 10^{-4}$. The statistical and systematic errors of P_{KK} have been assigned by performing a Monte Carlo simulation. All statistic errors have been considered gaussian while all the systematic errors as uniform. The result of the Monte Carlo error propagation can be seen in Figures 3.11 and 3.12.

Quantity	Value	$\sigma(x)$	$\Delta_{\mathrm{syst}}(x)$	Source
δ_{K}	0.384	0.001	0.006	measured
δ_{S}	0.387	0.001	$+0.010$ -0.009	simulated
δ_{HS}	0.401	0.001	$+0.010$ -0.009	simulated
δ_{e}	0.00203	0.00004	0.00005	simulated
δ_{IB}	0.0000579	0.0000011	$+0.0000019$ -0.0000033	simulated
ω_{K}	0.321		0.007	[11]
ω_{S}	0.383		0.007	[29]
ω_{HS}	0.383		0.007	[30]
P_{IB}	2.58×10^{-5}		0.04×10^{-5}	[12]
P_{KLLK}	3.16×10^{-4}		0.32×10^{-4}	[13]
N_{K}	6832441643	82659		measured
N_{peak}	1867184	1311		measured
N_{acc}	1718602	1366		measured
N_{true}	148582	2677		measured

Table 3.2: Quantities used for calculation of ^{55}Fe P_{KK}

Quantity	Value	Signal contribution (%)
$N^*_{\mathrm{HS,S}}$	999019688	97.45
$N^*_{\mathrm{HS,e}}$	3224293	0.31
$N^*_{\mathrm{S,e}}$	3036798	0.30
$N^{*\mathrm{SAuger}}_{\mathrm{HS,e}}$	9666337	0.94
$N^{*\mathrm{HSAuger}}_{\mathrm{S,e}}$	10249260	1.00

Table 3.3: Contributions to signal in ^{55}Fe P_{KK} calculation

Quantity	Value	Background contribution (%)
N_{acc}	1718602	99.745
$N_{\mathrm{K,IB}}$	10	0.001
$N_{\mathrm{K,e}}$	4384	0.254

Table 3.4: Contributions to background in the ^{55}Fe P_{KK} calculation
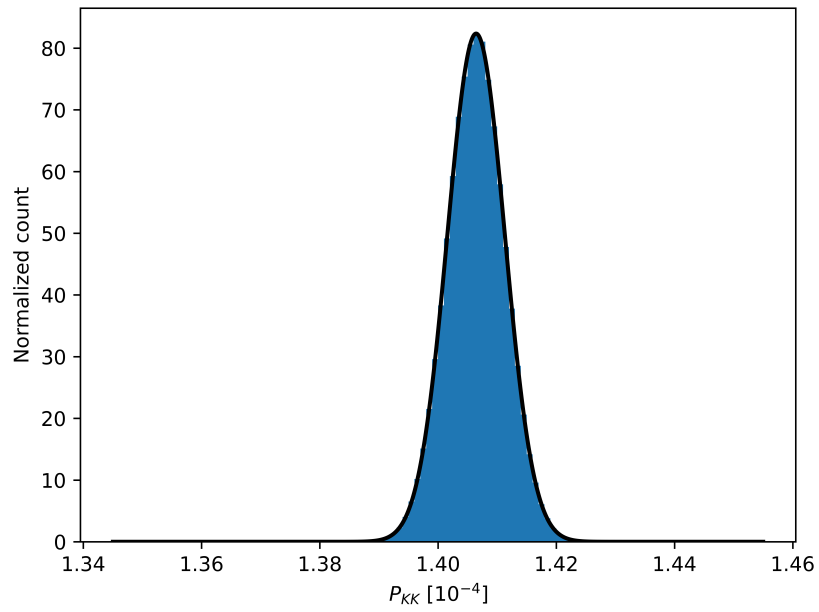
Figure 3.11: The result of a Monte Carlo error propagation of statistical error of ^{55}Fe P_{KK}. A gaussian function was fitted to the histogram with $\mu = 1.406$ and $\sigma = 0.005$.
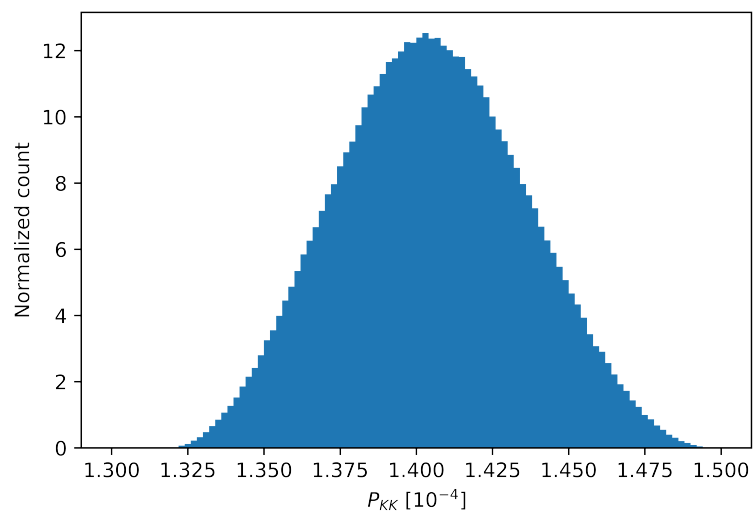

Figure 3.12: The result of a Monte Carlo propagation of systematic error of ^{55}Fe P_{KK}.

3.2.4 Discussion of P_{KK} result

The value of $P_{KK} = (1.406 \pm 005) \times 10^{-4}$ with the systematic error of $\Delta_{sys}(P_{KK})$ $= {}^{+0.030}_{-0.034} \times 10^{-4}$ has been measured. Bergmann et al. in 2016 [5] presented the value with currently highest precision $P_{KK} = (1.388 \pm 0.037) \times 10^{-4}$ with the systematic error of $\Delta_{sys}(P_{KK}) = 0.042 \times 10^{-4}$, using a pair of Timepix detectors. While the resulting values of P_{KK} agree on a 1σ level, the statistical error has been significantly improved thanks to using a pair of Timepix3 detectors. Measurement time has also significantly decreased from approximately two years to 13.5 days.
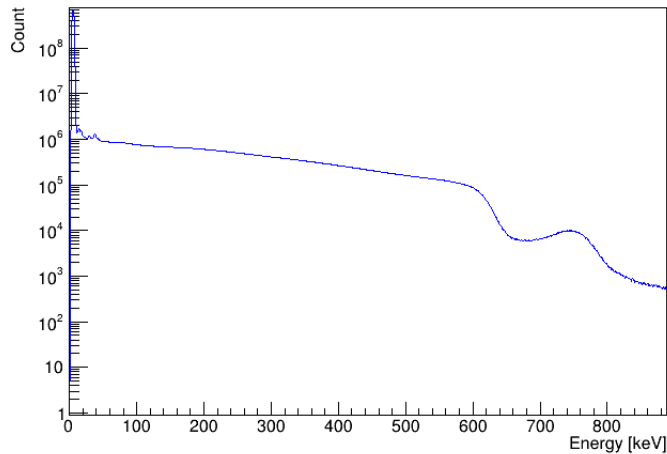
Figure 3.13: Measured energy spectrum of ^{54}Mn. The full energy peak at 835 keV and the Compton edge theoretically predicted at 639 keV are clearly visible

Quantity	Value	$\sigma(x)$	$\Delta_{syst}(x)$	Source
A [kBq]	141.8		0.5	measured
t [s]	2580936			measured
t [d]	29.8			measured
N_{meas}	2479518319		49795	measured
P_{K}	0.8896		0.0017	[16]
ω_{K}	0.289		0.005	[16]
δ_{K}	0.318	0.001	0.001	measured

Table 3.5: Quantities used for calculation of δ_{K}.

3.3 Measurement with ^{54}Mn source

Measurement with the ^{54}Mn source has been conducted using the same measurement setup as with the ^{55}Fe source. Information on the activity of the source has been supplied by the manufacturer and it was $A_0 = (141.8 \pm 0.5)$ kBq on November 1, 2014, 00:00. Total measurement time with the source amounted to 29.9 days. The energy spectrum of measured clusters can be seen in Figure 3.13.

In the same way, as in the measurement with the ^{55}Fe source, we can calculate the detection efficiency δ_{K} of the setup for K-line X-ray photons from daughter ^{54}Cr atom produced by K-shell electron capture decay of ^{54}Mn. We use Equation 3.1 for the calculation of δ_{K} and the same cut for N_{meas}, meaning we only consider clusters of energy in the region [3, 13] keV. The quantities used for the calculation and the result can be found in Table 3.5.

The value of δ_{K} for the setup stands at $\delta_{\mathrm{K}} = (0.318 \pm 0.001)$ with the systematic error $\Delta_{syst}(\delta_{\mathrm{K}}) = 0.001$ which was determined from the error of the activity of the source supplied by the manufacturer. The radioactive source's activity A was assumed to be constant for the calculation, and a value in the middle of the measurement time was chosen. The calculated value of δ_{K} was then used to calculate and plot the source's activity throughout the measurement. The result
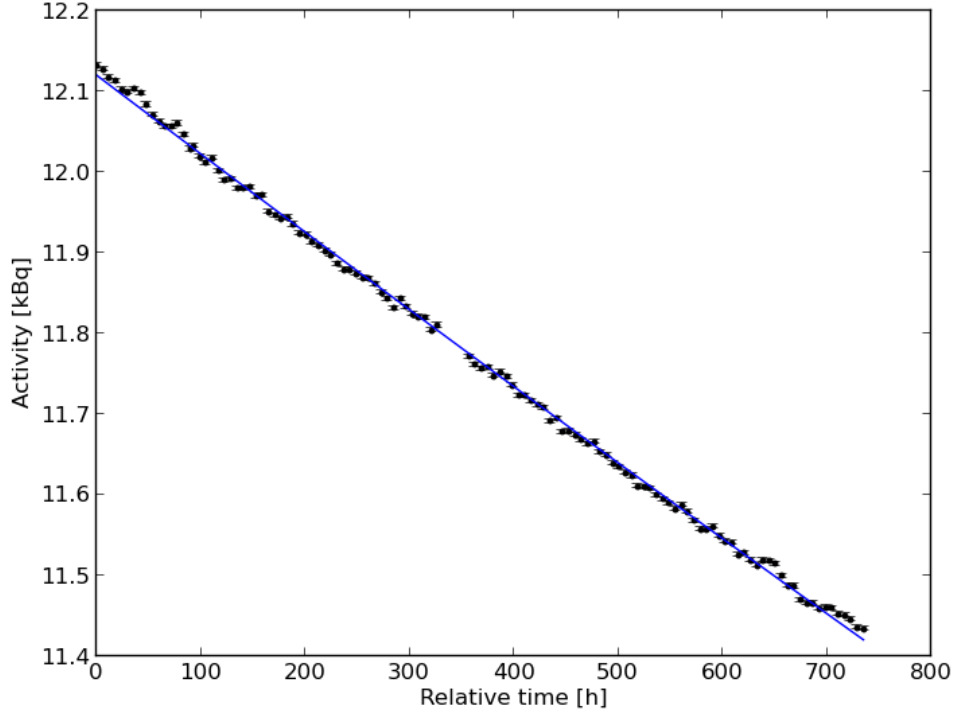
Figure 3.14: Measurement of the ^{54}Mn source activity with Timepix3 detectors. We fit an exponential $exp(ax + b)$ to the data with resulting coefficients: $a = (-8.09 \pm 0.76) \times 10^{-5}$, $b = (2.49 \pm 0.21)$.

is shown in Figure 3.14.

To be able to calculate P_{KK}, we will employ a similar approach as with the ^{55}Fe by utilizing the time spectrum of two coincident clusters shown in Figure 3.15, while recognizing all major processes contributing to signal and background.

Peaks of true coincidences ara clearly visible in the time spectrum in the region of ΔToA < 80 ns. By fitting a constant to the region of random coincidences, we can estimate their contribution to the region of true coincidences. We locate the endpoint of the region of true coincidences as the first bin of the histogram, in which the value is lower than the constant fit to the region of random coincidences $C = (2386 \pm 4)$. This way, we calculate the contribution of random coincidences to the region of true coincidences as $N_{\text{acc}} = (205101 \pm 453)$. The total number of coincidences in the true coincidences region is equal to $N_{\text{peak}} = (1086105 \pm 1042)$. The number can be calculated according to the equation 3.2 and is equal to $N_{\text{true}} = (881004 \pm 1495)$. We will utilize the number of true coincidences in the calculation of P_{KK}.

The peak in the time spectrum at the value of 30 ns can be attributed to a difference in drift time during coincident measurement of a K-line X-ray and a γ-ray. The measured timestamp t_{meas} is given by:

$$t_{\text{meas}} = t_{\text{interact}} + t_{\text{drift}} \tag{3.11}$$

where t_{interact} is the time when the particle interacts in the sensor and t_{drift} is the time that the holes take to drift to the pixelated side of the sensor. In case
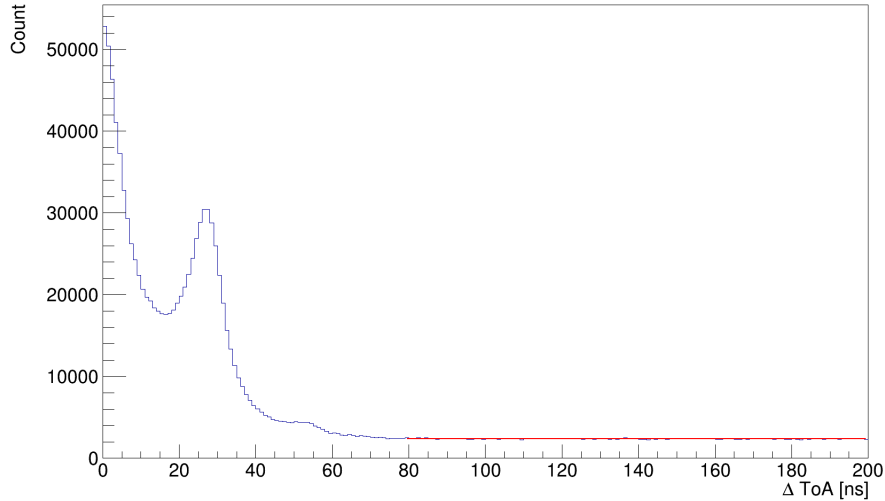
Figure 3.15: Time spectrum of two coincident clusters from ^{54}Mn. The spectrum was fitted by a constant in the flat region, with result $C = (2386 \pm 4)$, to estimate the number of accidental coincidences in the peak region of $\Delta\text{ToA} < 80$ ns. Only clusters with energy in the region [3, 13] keV are considered.

of coincident detection of a K-line X-ray and a γ-ray the time difference will be Δt (or ΔToA):

$$\Delta t = t^{\text{X}}_{\text{meas}} - t^{\gamma}_{\text{meas}} = t^{\gamma}_{\text{meas}} = (t^{\text{X}}_{\text{interact}} + t^{\text{X}}_{\text{drift}}) - (t^{\gamma}_{\text{interact}} + t^{\gamma}_{\text{drift}}) \qquad (3.12)$$

Since $t^{\gamma}_{\text{interact}} \approx t^{\text{X}}_{\text{interact}}$, Δt will be given by the difference in drift times of the K-line X-ray and the γ-ray. X-ray photons of 6 keV energy interact very soon after they enter the sensor, which in our measurement setup means close to the side of the common electrode. The holes created by this interaction then need to drift through almost the whole sensor. In the case of a 0.5 mm thick Si sensor and 230 V bias voltage applied, this means 30 ns drift time according to measurements conducted by Bergmann [27]. The γ-rays interact anywhere due to their high energy and can even penetrate the sensor. However, interactions close to the pixelated side have a large probability to lie within the required energy range of 3-13 keV: In addition to the low energy Compton electrons, here additionally electrons leaving the sensor are counted. In that case, their drift time will be almost 0. This means that pairs of K-line photon and γ-ray measured in coincidence and passing the energy cut should have:

$$\Delta t \approx t^{\text{X}}_{\text{drift}} - t^{\gamma}_{\text{drift}} \approx 30ns$$

This results in the peak-like structure at 30 ns seen in the time spectrum. Since no additional γ-ray is emitted in the electron capture decay ^{55}Fe, there is no second peak in Figure 3.6.

The discernible edge at $\approx$55 ns in the time spectrum is probably due to an incomplete compensation of the time-walk in some of the pixels.

32

3.3.1 Derivation of methodology for calculation of ^{54}Mn P_{KK}

Processes leading to an empty K-shell

We first consider the signal process, K-shell electron capture where through electron-electron interaction the second K-shell electron is removed from the atom. Four particles are emitted in such case, and we can assume $P_\gamma = 1$.

The first contribution comes from the detection of the hypersatellite photon together with the satellite photon, while the γ photon and the shake-off electrons are not detected:

$$N_{\text{HS,S}} = A(t)t\, P_{\text{K}} P_{\text{KK}}\, \delta_{\text{HS}}\delta_{\text{S}}(1 - \delta_{\text{e}})(1 - \delta_\gamma)\,\omega_{\text{HS}}\omega_{\text{S}} \tag{3.13}$$

With $N_{\text{K}} = P_{\text{K}}\omega_{\text{K}}\delta_{\text{K}}A(t)t$, we get:

$$A(t)t = \frac{N_{\text{K}}}{P_{\text{K}}\omega_{\text{K}}\delta_{\text{K}}} \tag{3.14}$$

Inserting 3.14 into equation 3.13 gives:

$$N_{\text{HS,S}} = \frac{P_{\text{KK}}N_{\text{K}}}{\omega_{\text{K}}\delta_{\text{K}}}\delta_{HS}\delta_{S}(1 - \delta_{\text{e}})(1 - \delta_\gamma)\,\omega_{\text{HS}}\omega_{\text{S}} \tag{3.15}$$

Analogously, we obtain twelve other contributions:

$$N_{\text{e,HS}} = \frac{P_{\text{KK}}N_{\text{K}}}{\omega_{\text{K}}\delta_{\text{K}}}\delta_{\text{HS}}(1 - \delta_{\text{S}})\delta_{\text{e}}(1 - \delta_\gamma)\,\omega_{\text{HS}}\omega_{\text{S}} \tag{3.16}$$

$$N_{\text{e,S}} = \frac{P_{\text{KK}}N_{\text{K}}}{\omega_{\text{K}}\delta_{\text{K}}}(1 - \delta_{\text{HS}})\delta_{\text{S}}\delta_{\text{e}}(1 - \delta_\gamma)\,\omega_{\text{HS}}\omega_{\text{S}} \tag{3.17}$$

$$N_{\gamma,\text{HS}} = \frac{P_{\text{KK}}N_{\text{K}}}{\omega_{\text{K}}\delta_{\text{K}}}\delta_{\text{HS}}(1 - \delta_{\text{S}})(1 - \delta_{\text{e}})\delta_\gamma\,\omega_{\text{HS}}\omega_{\text{S}} \tag{3.18}$$

$$N_{\gamma,\text{S}} = \frac{P_{\text{KK}}N_{\text{K}}}{\omega_{\text{K}}\delta_{\text{K}}}(1 - \delta_{\text{HS}})\delta_{\text{S}}(1 - \delta_{\text{e}})\delta_\gamma\,\omega_{\text{HS}}\omega_{\text{S}} \tag{3.19}$$

$$N_{\gamma,\text{e}} = \frac{P_{\text{KK}}N_{\text{K}}}{\omega_{\text{K}}\delta_{\text{K}}}(1 - \delta_{\text{HS}})(1 - \delta_{\text{S}})\delta_{\text{e}}\delta_\gamma\,\omega_{\text{HS}}\omega_{\text{S}} \tag{3.20}$$

$$N_{\gamma,\text{S}}^{\text{HS Auger}} = \frac{P_{\text{KK}}N_{\text{K}}}{\omega_{\text{K}}\delta_{\text{K}}}\delta_{\text{S}}(1 - \delta_{\text{e}})\delta_\gamma\,(1 - \omega_{\text{HS}})\omega_{\text{S}} \tag{3.21}$$

$$N_{\text{e,S}}^{\text{HS Auger}} = \frac{P_{\text{KK}}N_{\text{K}}}{\omega_{\text{K}}\delta_{\text{K}}}\delta_{\text{S}}\delta_{\text{e}}(1 - \delta_\gamma)\,(1 - \omega_{\text{HS}})\omega_{\text{S}} \tag{3.22}$$

$$N_{\gamma,\text{e}}^{\text{HS Auger}} = \frac{P_{\text{KK}}N_{\text{K}}}{\omega_{\text{K}}\delta_{\text{K}}}(1 - \delta_{\text{S}})\delta_{\text{e}}\delta_\gamma\,(1 - \omega_{\text{HS}})\omega_{\text{S}} \tag{3.23}$$

$$N_{\gamma,\text{HS}}^{\text{S Auger}} = \frac{P_{\text{KK}}N_{\text{K}}}{\omega_{\text{K}}\delta_{\text{K}}}\delta_{\text{HS}}(1 - \delta_{\text{e}})\delta_\gamma\,\omega_{\text{HS}}(1 - \omega_{\text{S}}) \tag{3.24}$$

$$N_{\text{e,HS}}^{\text{S Auger}} = \frac{P_{\text{KK}}N_{\text{K}}}{\omega_{\text{K}}\delta_{\text{K}}}\delta_{\text{HS}}\delta_{\text{e}}(1 - \delta_\gamma)\,\omega_{\text{HS}}(1 - \omega_{\text{S}}) \tag{3.25}$$

$$N_{\gamma,\text{e}}^{\text{S Auger}} = \frac{P_{\text{KK}}N_{\text{K}}}{\omega_{\text{K}}\delta_{\text{K}}}(1 - \delta_{\text{HS}})\delta_{\text{e}}\delta_\gamma\,\omega_{\text{HS}}(1 - \omega_{\text{S}}) \tag{3.26}$$

$$N_{\gamma,\text{e}}^{\text{HS,S Auger}} = \frac{P_{\text{KK}}N_{\text{K}}}{\omega_{\text{K}}\delta_{\text{K}}}\delta_{\text{e}}\delta_\gamma\,(1 - \omega_{\text{HS}})(1 - \omega_{\text{S}}) \tag{3.27}$$

Summing up all individual contributions results in:

$$N_{\mathrm{KK}} = \frac{P_{\mathrm{KK}} N_{\mathrm{K}}}{\omega_{\mathrm{K}} \delta_{\mathrm{K}}} \times \Delta_{\mathrm{KK}} \tag{3.28}$$

where Δ_{KK} denotes the sum of the different combinations of $\delta_{\mathrm{HS}}, \delta_{\mathrm{S}}, \delta_{\mathrm{e}}, \delta_{\gamma}, \omega_{\mathrm{HS}}$, and ω_{K}.

The second set of equations is due to the internal conversion of the K-shell electron. In this case, three particles are emitted in coincidence: the conversion electron with an energy of $829 \, \mathrm{keV}$, the hypersatellite and the satellite photons. We find:

$$N_{\mathrm{HS,S}} = A(t)t \, P_{\mathrm{K}} \alpha_{\mathrm{K}} \, \delta_{\mathrm{HS}} \delta_{\mathrm{S}} (1 - \delta_{\mathrm{IC}}) \, \omega_{HS} \omega_S = \frac{\alpha_{\mathrm{K}} N_{\mathrm{K}}}{\omega_{\mathrm{K}} \delta_{\mathrm{K}}} \delta_{\mathrm{HS}} \delta_{S} (1 - \delta_{\mathrm{IC}}) \, \omega_{\mathrm{HS}} \omega_S \tag{3.29}$$

and analogously, we find the other combinations:

$$N_{\mathrm{HS,e}} = \frac{\alpha_{\mathrm{K}} N_{\mathrm{K}}}{\omega_{\mathrm{K}} \delta_{\mathrm{K}}} \delta_{\mathrm{HS}} (1 - \delta_S) \delta_{\mathrm{IC}} \, \omega_{\mathrm{HS}} \omega_S \tag{3.30}$$

$$N_{\mathrm{S,e}} = \frac{\alpha_{\mathrm{K}} N_{\mathrm{K}}}{\omega_{\mathrm{K}} \delta_{\mathrm{K}}} (1 - \delta_{\mathrm{HS}}) \delta_S \delta_{\mathrm{IC}} \, \omega_{\mathrm{HS}} \omega_S \tag{3.31}$$

$$N_{\mathrm{HS,e}}^{\mathrm{S \, Auger}} = \frac{\alpha_{\mathrm{K}} N_{\mathrm{K}}}{\omega_{\mathrm{K}} \delta_{\mathrm{K}}} \delta_{\mathrm{HS}} \delta_{\mathrm{IC}} \, \omega_{\mathrm{HS}} (1 - \omega_S) \tag{3.32}$$

$$N_{\mathrm{HS,e}}^{\mathrm{HS \, Auger}} = \frac{\alpha_{\mathrm{K}} N_{\mathrm{K}}}{\omega_{\mathrm{K}} \delta_{\mathrm{K}}} \delta_S \delta_{\mathrm{IC}} (1 - \omega_{\mathrm{HS}}) \omega_S, \tag{3.33}$$

which sum up to:

$$N_{\mathrm{IC}}^{\mathrm{K-shell}} = \frac{\alpha_{\mathrm{K}} N_{\mathrm{K}}}{\omega_{\mathrm{K}} \delta_{\mathrm{K}}} \times \Delta_{\mathrm{IC}}^{\mathrm{K-shell}} \tag{3.34}$$

we can again denote the sum of the combinations of δ_i and ω_i as $\Delta_{\mathrm{IC}}^{\mathrm{K-shell}}$.

Background processes involving a K-shell and an L-shell vacancy

Internal conversion on higher shells (L, M) leads to the creation of an atom in the state with a K-shell vacancy and an L/M-shell vacancy, which decays through the emission of a satellite photon, which can mimic the signal if measured together with the internal conversion electron. We find:

$$N_{\mathrm{LM-IC}}^{\mathrm{K-capture}} = A(t)t \, P_{\mathrm{K}} \alpha_{\mathrm{LM}} \, \delta_S \delta_{\mathrm{IC}} \, \omega_S = \frac{N_{\mathrm{K}}}{\omega_{\mathrm{K}} \delta_{\mathrm{K}}} \alpha_{\mathrm{LM}} \delta_S \delta_{\mathrm{IC}} \, \omega_S. \tag{3.35}$$

And likewise, higher shell electron capture with internal conversion electron on the K-shell:

$$N_{\mathrm{K-IC}}^{\mathrm{LM-capture}} = A(t)t \, P_{\mathrm{LM}} \alpha_{\mathrm{K}} \, \delta_S \delta_{\mathrm{IC}} \, \omega_S = \frac{N_{\mathrm{K}}}{P_{\mathrm{K}} \omega_{\mathrm{K}} \delta_{\mathrm{K}}} P_{\mathrm{LM}} \alpha_{\mathrm{K}} \delta_S \delta_{\mathrm{IC}} \, \omega_S. \tag{3.36}$$

Adding equations 3.35 and 3.36 gives:

$$N_{\mathrm{IC}}^{\mathrm{KLLK}} = \frac{N_{\mathrm{K}}}{\omega_{\mathrm{K}} \delta_{\mathrm{K}}} \left(\alpha_{\mathrm{LM}} + \frac{P_{\mathrm{LM}}}{P_{\mathrm{K}}} \alpha_{\mathrm{K}} \right) \Delta_{\mathrm{IC}}^{\mathrm{KLLK}}, \tag{3.37}$$

with $\Delta_{\text{IC}}^{\text{KLLK}} = \delta_{\text{S}}\delta_{\text{IC}}\omega_{\text{S}}$.

The second set of processes leading to a K- and L-shell vacancy state is K-capture followed by L-shake off ("KL") or vice versa. In such case, three particles are emitted in coincidence: a shake-off electron, γ photon from the nucleus, and a satellite photon. We find the following combinations:

$$N_{\text{e,S}}^{\text{KL}} = \frac{N_{\text{K}}}{P_{\text{K}}\omega_{\text{K}}\delta_{\text{K}}} P_{\text{eL}}P_{\text{K}}\,\delta_{\text{S}}\delta_{\text{KL}}(1-\delta_{\gamma})\,\omega_S \tag{3.38}$$

$$N_{\gamma,\text{e}}^{\text{KL}} = \frac{N_{\text{K}}}{P_{\text{K}}\omega_{\text{K}}\delta_{\text{K}}} P_{\text{eL}}P_{\text{K}}\,(1-\delta_{\text{S}})\delta_{\text{KL}}\delta_{\gamma}\,\omega_S \tag{3.39}$$

$$N_{\gamma,\text{S}}^{\text{KL}} = \frac{N_{\text{K}}}{P_{\text{K}}\omega_{\text{K}}\delta_{\text{K}}} P_{\text{eL}}P_{\text{K}}\,\delta_{\text{S}}(1-\delta_{\text{KL}})\delta_{\gamma}\,\omega_S \tag{3.40}$$

$$N_{\gamma,\text{e}}^{\text{KL, S Auger}} = \frac{N_{\text{K}}}{P_{\text{K}}\omega_{\text{K}}\delta_{\text{K}}} P_{\text{eL}}P_{\text{K}}\,\delta_{\text{KL}}\delta_{\gamma}\,(1-\omega_S) \tag{3.41}$$

$$N_{\text{e,S}}^{\text{LK}} = \frac{N_{\text{K}}}{P_{\text{K}}\omega_{\text{K}}\delta_{\text{K}}} P_{\text{eK}}P_{\text{L}}\,\delta_{\text{S}}\delta_{\text{LK}}(1-\delta_{\gamma})\,\omega_S \tag{3.42}$$

$$N_{\gamma,\text{e}}^{\text{LK}} = \frac{N_{\text{K}}}{P_{\text{K}}\omega_{\text{K}}\delta_{\text{K}}} P_{\text{eK}}P_{\text{L}}\,(1-\delta_{\text{S}})\delta_{\text{LK}}\delta_{\gamma}\,\omega_S \tag{3.43}$$

$$N_{\gamma,\text{S}}^{\text{LK}} = \frac{N_{\text{K}}}{P_{\text{K}}\omega_{\text{K}}\delta_{\text{K}}} P_{\text{eK}}P_{\text{L}}\,\delta_{\text{S}}(1-\delta_{\text{LK}})\delta_{\gamma}\,\omega_S \tag{3.44}$$

$$N_{\gamma,\text{e}}^{\text{LK, S Auger}} = \frac{N_{\text{K}}}{P_{\text{K}}\omega_{\text{K}}\delta_{\text{K}}} P_{\text{eK}}P_{\text{L}}\,\delta_{\text{LK}}\delta_{\gamma}\,(1-\omega_S) \tag{3.45}$$

$$\tag{3.46}$$

where P_{eK} and P_{eL} are probabilities of K-shell and L-shell shake-off electrons emission. With $\delta_{\text{KL}} = \delta_{\text{LK}} = \delta_{\text{e}}$, it can be simplified to

$$N_{\text{KLLK}} = \frac{N_K}{P_{\text{K}}\omega_{\text{K}}\delta_{\text{K}}}(P_{\text{eK}}P_{\text{L}} + P_{\text{eL}}P_{\text{K}})\,\Delta_{\text{KLLK}} \tag{3.47}$$

Processes with isolated K-shell vacancies

The most important decay-related background is the coincident detection of the γ photon with the K-line X-ray photon emitted during the electron capture decay:

$$N_{\gamma,\text{K}} = A(t)t\,P_{\text{K}}\delta_{\text{K}}\delta_{\gamma}\omega_{\text{K}} = N_{\text{K}}\delta_{\gamma} \tag{3.48}$$

Secondly, we consider the combination of the internal bremsstrahlung photon with either the K-line X-ray photon or the γ photon. We find the following combinations:

$$N_{\text{IB,K}} = A(t)t\,P_{\text{K}}P_{IB}\,\delta_{\text{K}}\delta_{\text{IB}}(1-\delta_{\gamma})\,\omega_{\text{K}} \quad = N_{\text{K}}P_{\text{IB}}\delta_{IB}\delta_{\gamma}(\frac{1}{\delta_{\gamma}}-1) \tag{3.49}$$

$$N_{\gamma,\text{IB}} = A(t)t\,P_{\text{K}}P_{IB}\,(1-\delta_{\text{K}})\delta_{\text{IB}}\delta_{\gamma}\,\omega_{\text{K}} \quad = N_{\text{K}}P_{\text{IB}}\delta_{IB}\delta_{\gamma}(\frac{1}{\delta_{\text{K}}}-1) \tag{3.50}$$

$$N_{\gamma,\text{K}} = A(t)t\,P_{\text{K}}P_{IB}\,\delta_{\text{K}}(1-\delta_{\text{IB}})\delta_{\gamma}\,\omega_{\text{K}} \quad = N_{\text{K}}P_{\text{IB}}\delta_{IB}\delta_{\gamma}(\frac{1}{\delta_{IB}}-1) \tag{3.51}$$

$$N_{\gamma,\text{IB}}^{\text{K-Auger}} = A(t)t\,P_{\text{K}}P_{IB}\,\delta_{\text{IB}}\delta_{\gamma}(1-\omega_{\text{K}}) \quad = N_{\text{K}}P_{\text{IB}}\delta_{IB}\delta_{\gamma}(\frac{1}{\omega_{\text{K}}}-1) \tag{3.52}$$

By summing all these contributions together, we find:

$$N_{\text{IB}} = N_{\text{K}}\delta_{\text{IB}}P_{\text{IB}}\delta_\gamma \left(\frac{1}{\delta_\gamma} + \frac{1}{\delta_{\text{IB}}} + \frac{1}{\delta_{\text{K}}} + \frac{1}{\omega_{\text{K}}} - 4 \right) = N_{\text{K}}P_{\text{IB}}\Delta_{\text{IB}}. \qquad (3.53)$$

The last contribution to the background is the detection of two K-shell X-ray photons from two separate K-shell electron capture decays. We denote its contribution as N_{acc} and calculate it from fitting a straight line to the flat part of the time spectrum as shown in Figure 3.15.

With all the signal and background processes considered, we can now derive the final formula for the calculation of P_{KK}:

$$
\begin{aligned}
N_{\text{peak}} &= \frac{P_{\text{KK}}N_{\text{K}}}{\omega_{\text{K}}\delta_{\text{K}}}\Delta_{\text{KK}} + \frac{\alpha_{\text{K}}N_{\text{K}}}{\omega_{\text{K}}\delta_{\text{K}}\Delta_{\text{IC}}^{\text{K}}} + \frac{N_{\text{K}}}{\omega_{\text{K}}\delta_{\text{K}}}\left(\alpha_{\text{LM}} + \frac{P_{\text{LM}}}{P_{\text{K}}}\alpha_{\text{K}} \right)\Delta_{\text{IC}}^{\text{KLLK}} \\
&+ \frac{N_{\text{K}}}{\omega_{\text{K}}\delta_{\text{K}}}\left(\frac{P_{\text{eK}}P_{\text{L}}}{P_{\text{K}}} + P_{\text{eL}} \right)\Delta_{\text{KLLK}} + N_{\text{K}}\delta_\gamma + N_{\text{K}}P_{\text{IB}}\Delta_{\text{IB}} - N_{\text{acc}} \quad (3.54)
\end{aligned}
$$

$$
\begin{aligned}
P_{\text{KK}} &= \frac{\omega_{\text{K}}\delta_{\text{K}}}{\Delta_{\text{KK}}}\left(\frac{N_{\text{true}}}{N_{\text{K}}} - \delta_\gamma - P_{\text{IB}}\Delta_{\text{IB}} \right) - \left(\alpha_{\text{LM}} + \frac{P_{\text{LM}}}{P_{\text{K}}}\alpha_{\text{K}} \right)\frac{\Delta_{\text{IC}}^{\text{KLLK}}}{\Delta_{\text{KK}}} - \\
&- \alpha_{\text{K}}\frac{\Delta_{\text{IC}}^{\text{K}}}{\Delta_{\text{KK}}} - \left(\frac{P_{\text{eK}}P_{\text{L}}}{P_{\text{K}}} + P_{\text{eL}} \right)\frac{\Delta_{\text{KLLK}}}{\Delta_{\text{KK}}} \qquad\qquad (3.55)
\end{aligned}
$$

3.3.2 Optimization of setup in the simulation framework

The same way as in the case of ^{55}Fe source, we use the K-line photons signal to optimize the geometry of the measurement setup within the Allpix^2 simulation framework. A comparison of the structure of pixel hits from simulation, and measurement is shown in Figures 3.16 - 3.19.

The measured detection efficiency of K-line X-rays is $\delta_{\text{K}} = (0.318 \pm 0.001)$. After optimization of the simulation setup, the simulated detection efficiency was $\delta_{\text{K}}^{\text{sim}} = (0.317 \pm 0.001)$. The energy of K-line X-ray photons within the simulation was set to be 5.53 keV as a weighted average of value taken from [16].
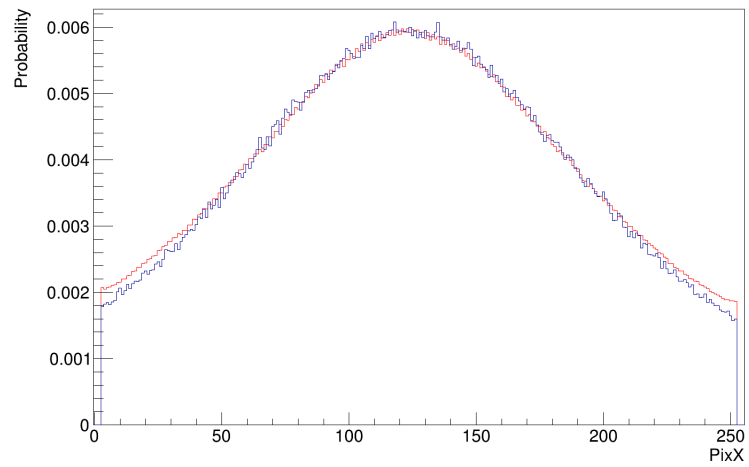
Figure 3.16: Comparison of measured and simulated pixel hits data. Projection to the X axis in layer 1. The blue line corresponds to simulated data, while the red to measured data.
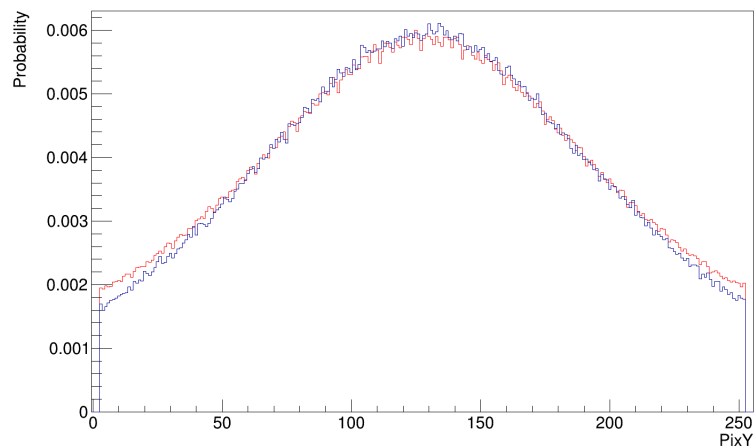
Figure 3.17: Comparison of measured and simulated pixel hits data. Projection to the Y axis in layer 1. The blue line corresponds to simulated data, while the red to measured data.
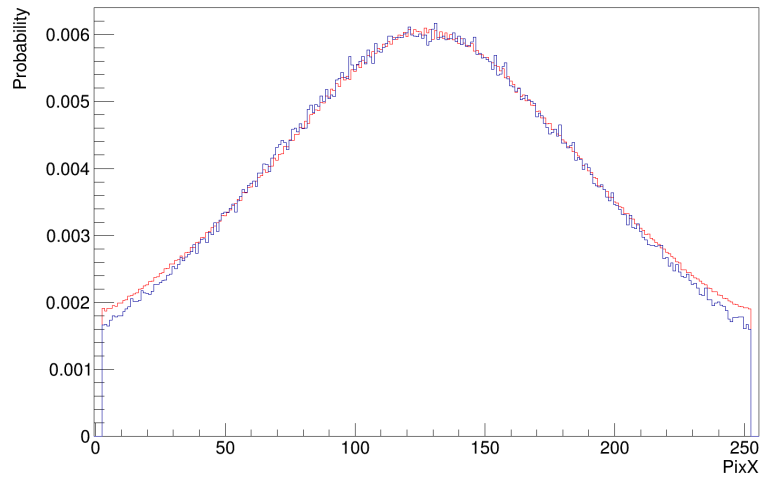
Figure 3.18: Comparison of measured and simulated pixel hits data. Projection to the X axis in layer 2. The blue line corresponds to simulated data, while the red to measured data.
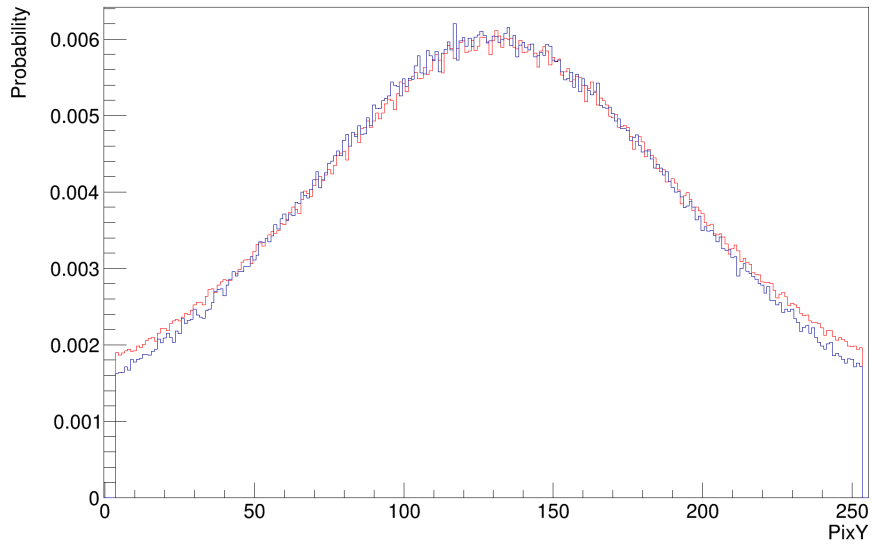
Figure 3.19: Comparison of measured and simulated pixel hits data. Projection to the Y axis in layer 2. The blue line corresponds to simulated data, while the red to measured data.

Following detection efficiencies were simulated using the optimized simulation setup:

- δ_S - detection efficiency for satellite photons. their energy was set at 5.58 keV [10]

- δ_HS - detection efficiency for hypersatellite photons. their energy was set at 5.77 keV [10]

- δ_e - detection efficiency for shake-off electrons, their energy was set as a spectrum taken from [15] and properly scaled to reflect the higher endpoint of the spectrum.

- δ_IB - detection efficiency for internal bremsstrahlung photons, their energy was set as a spectrum taken from [17]

- δ_IC - detection efficiency for internal conversion electrons, their energy was set at 829 keV

- δ_γ - detection efficiency for γ photons was set at 834.9 keV

The resulting values of simulated detection efficiencies are summarized in Table 3.6 in the following section.

3.3.3 Calculation of P_KK

Values of all quantities needed for calculation of ^{54}Mn P_KK can be found in Table 3.6.

The P_KK value for ^{54}Mn amounts to:

$$P_\mathrm{KK} = (3.93 \pm 0.44) \times 10^{-4}$$

with systematic error of $\Delta_\mathrm{sys}(P_\mathrm{KK}) = {}^{+0.25}_{-1.11} \times 10^{-4}$. The statistical and systematic errors of P_KK have been assigned by performing a Monte Carlo error propagation. All statistic errors have been considered gaussian, while all the systematic errors as uniform. Results of the Monte Carlo simulation can be seen in Figures 3.20 and 3.21.

Quantity	Value	$\sigma(x)$	$\sigma_{syst}(x)$	Source
δ_{K}	0.318	0.001	0.001	simulated
δ_{S}	0.321	0.001	$^{+0.008}_{-0.010}$	simulated
δ_{HS}	0.336	0.001	$^{+0.008}_{-0.009}$	simulated
δ_{e}	0.00195	0.00004	$^{+0.00002}_{-0.00001}$	simulated
δ_{IB}	0.0000566	0.0000011	$^{+0.0000024}_{-0.0000022}$	simulated
δ_{γ}	0.000282	0.000005	$^{+0.000017}_{-0.000006}$	simulated
δ_{IC}	0.00602	0.00011	$^{+0.00012}_{-0.00009}$	simulated
ω_{K}	0.289		0.005	[16]
ω_{S}	0.305		0.005	extrapolated
ω_{HS}	0.310		0.005	extrapolated
P_{K}	0.8896		0.0017	[16]
P_{L}	0.0948		0.0002	[16]
P_{IB}	6.5×10^{-5}		1.5×10^{-5}	[17]
P_{IC}	2.45×10^{-4}		0.04×10^{-4}	[16]
P_{eK}	3.99×10^{-4}		0.20×10^{-4}	interpolated
P_{eL}	0.43×10^{-4}		0.02×10^{-4}	interpolated
α_{K}	2.22×10^{-4}		0.04×10^{-4}	[16]
α_{LM}	0.233×10^{-4}		0.034×10^{-4}	[16]
N_{peak}	1086105	1042		measured
N_{acc}	205101	453		measured
N_{true}	881004	1495		measured
N_{K}	2479518319	49795		measured

Table 3.6: Quantities used for calculation of ^{54}Mn P_{KK}
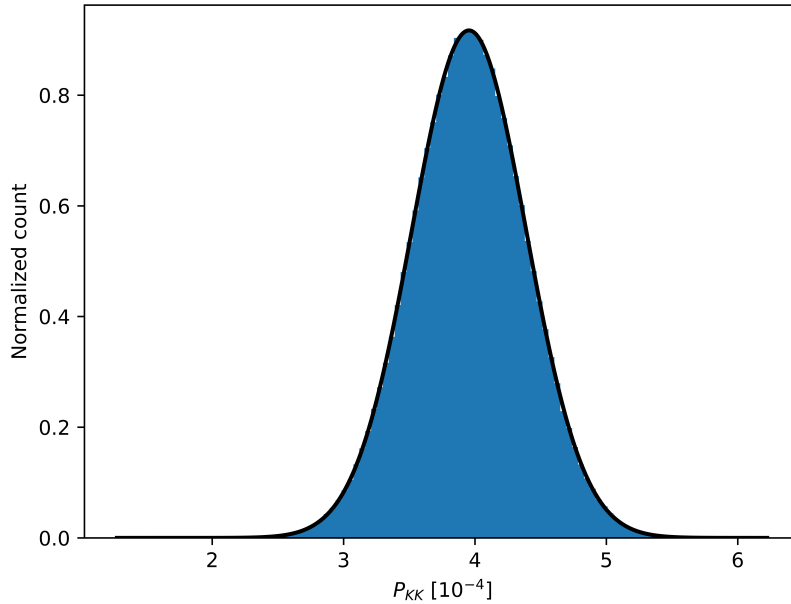
Figure 3.20: Result of Monte Carlo error propagation of statistical error of ^{54}Mn P_{KK}. A gaussian function was fitted to the histogram with $\mu = 3.93$ and $\sigma = 0.44$.
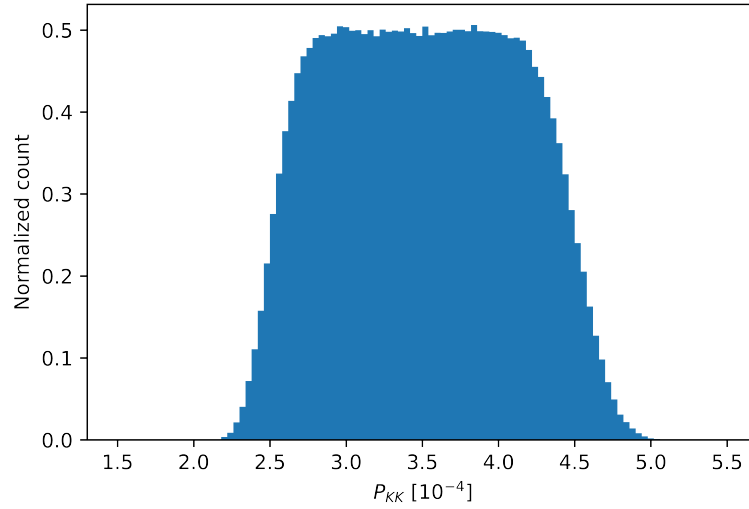
Figure 3.21: Result of Monte Carlo error propagation of systematic error of ^{54}Mn P_{KK}.

3.3.4 Discussion of P_{KK} result

The value of $P_{\mathrm{KK}} = (3.93 \pm 0.44) \times 10^{-4}$ with systematic error of $\Delta_{\mathrm{sys}}(P_{\mathrm{KK}}) = {}^{+0.25}_{-1.11}$ $\times 10^{-4}$ has been measured. When comparing the achieved result to the value measured in 1984 by Nagy and Schupp $P_{\mathrm{KK}} = (3.6 \pm 0.3) \times 10^{-4}$ [6], we find that the results agree on 1σ level. When comparing it to the value measured in 2003 by Hindi $P_{\mathrm{KK}} = (2.3 \pm {}^{+0.8}_{-0.5}) \times 10^{-4}$ [7], we find that the results agree on 2σ level. The errors of P_{KK} are mostly given by the errors of δ_γ since the coincident detection of a K-line X-ray and a γ-ray is on the same level of magnitude as the signal. A triple coincidence measurement is recommended for the future to completely avoid this background process.
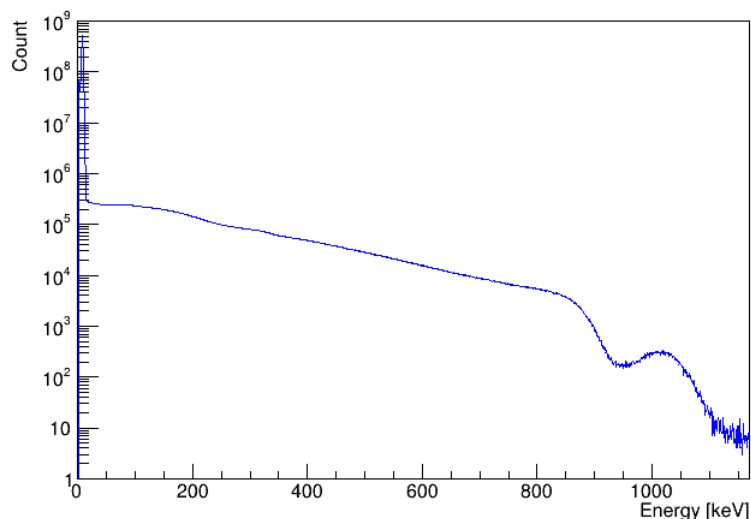
Figure 3.22: Measured energy spectrum of ^{65}Zn. Full energy peak and the Compton edge theoretically predicted at 908 keV are clearly visible

Quantity	Value	$\sigma(x)$	$\Delta_{syst}(x)$	Source
A [kBq]	7.94		0.56	measured
t [s]	1634571			measured
t [d]	18.9			measured
N_{meas}	2003987955		44766	measured
P_{K}	0.8823		0.0017	[18]
ω_{K}	0.454		0.004	[18]
δ_{K}	0.385	0.001	0.003	measured

Table 3.7: Quantities used for calculation of δ_{K}.

3.4 Measurement with ^{65}Zn source

Measurement with the ^{65}Zn source has been conducted using the same measurement setup as in the case of the previous two sources. The activity of the ^{65}Zn source was set to be $A_0 = (213.7 \pm 1.5)$ kBq on November 1, 2014, 00:00. Total measurement time with the source amounted to 18.9 days. The energy spectrum of measured clusters can be seen in Figure 3.22.

In the same way, as in the measurement with the previous two sources, we can calculate detection efficiency δ_{K} of the setup for K-line X-ray photons from daughter ^{65}Cu atom produced by K-shell electron capture decay or β^+ decay of ^{65}Zn. We use Equation 3.1 for the calculation of δ_{K} and the same cut for N_{meas}, meaning we only consider clusters of energy in the region [3, 13] keV. Quantities used for the calculation and the result can be found in Table 3.7.

The value of δ_{K} for the setup stands at $\delta_{\mathrm{K}} = (0.385 \pm 0.001)$ with the systematic error $\Delta_{syst}(\delta_{\mathrm{K}}) = 0.003$. The radioactive source's activity A was assumed to be constant for the calculation and a value in the middle of the measurement time was chosen. The calculated value of δ_{K} was then used to calculate and plot the source's activity throughout the measurement. The result is shown in Figure
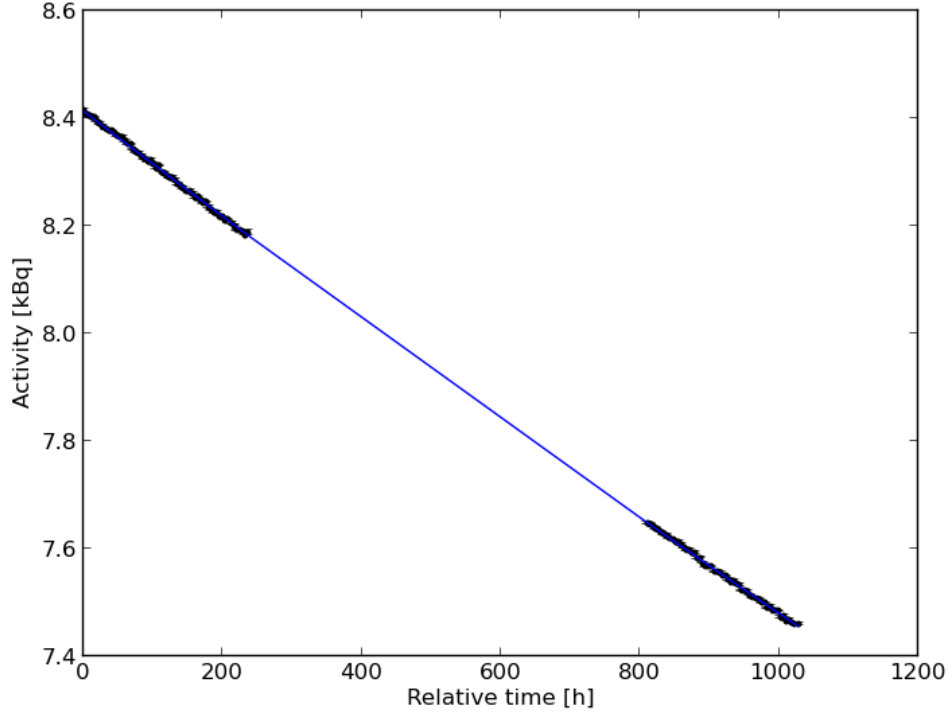
Figure 3.23: Measurement of the ^{65}Zn source activity with Timepix3 detectors. The measurement has been done in two runs with a pause in the middle. We fit an exponential $exp(ax + b)$ to the data with resulting coefficients: $a = (-1.17 \pm 0.03) \times 10^{-4}$, $b = (2.13 \pm 0.05)$.

3.23.

To be able to calculate P_{KK}, we would employ a similar approach as with the previous two isotopes by utilizing the time spectrum of two coincident clusters shown in Figure 3.24, while recognizing all major processes contributing to signal and background.

The peak at 40 ns in the time spectrum and the edge at 65 ns can be attributed to the same effects as in the case of ^{54}Mn time spectrum. Only this time, they are shifted by 10 ns in the positive direction. This is caused by a different bias voltage used during the measurement with the ^{65}Zn source. Instead of the 230 V bias voltage used with the previous source, 150 V bias voltage is used in the measurement with the current source. In the case of a 0.5 mm thick Si sensor and 150 V bias voltage applied, a maximum drift time of 40 ns is expected according to the measurements conducted by Bergmann [27]. That means due to the change of the bias voltage, the peak and the edge are shifted approximately by 10 ns in the positive direction.

In the case of employing a similar approach to the calculation of P_{KK} as with the previous two isotopes. ^{65}Zn decays in 48.35% of cases straight to a stable state of ^{65}Cu, in such cases, the behaviour is the same as in electron capture decay of ^{55}Fe. In 50.23 % of decays of ^{65}Zn behaves as ^{54}Mn since the additional transition from state 5/2⁻ to state 1/2⁻ is almost negligible. Nevertheless, detection efficiencies δ_S, δ_{HS}, δ_e, δ_γ, δ_{IC} and δ_{IB} would need to be simulated using
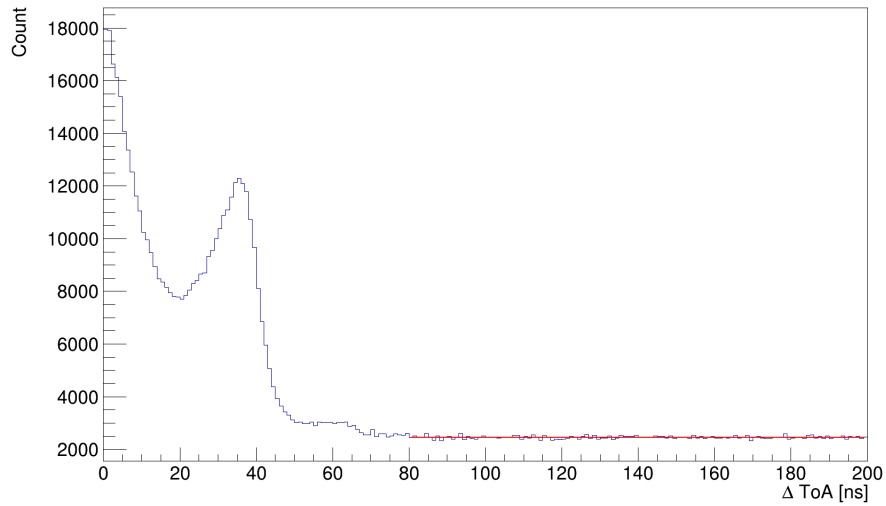
Figure 3.24: Time spectrum of two coincident clusters from ^{65}Zn. The spectrum was fitted by a constant in the flat region, with result $C = 2386$, to estimate the number of accidental coincidences in the peak region of ΔToA $<$ 20 ns.

an optimized simulation setup. The methodology for calculation of contributions of background processes due to β^+ decay of ^{65}Zn would need to be developed. A triple coincidence measurement would be the recommended approach to limit the number of coincident processes needed to be considered and to eliminate the effect of high background contribution of coincident detection of a K-line X-ray and a γ-ray.

Conclusion

Experimental studies of the K-shell double vacancy production in the electron capture decays of ^{55}Fe, ^{54}Mn, ^{65}Zn using a pair of Timepix3 detectors have been carried out. Measured data have been preprocessed and explored. The methodology for calculation of P_{KK} in ^{55}Fe and ^{54}Mn has been developed. Simulations using Allpix^2 framework have been carried out to determine detection efficiencies of the measurement setup for particles participating in processes coincident with electron capture decay of ^{55}Fe and ^{54}Mn. Value of $P_{KK} = (1.406 \pm 0.005) \times 10^{-4}$ with the systematic error of $\Delta_{sys}(P_{KK}) =^{+0.030}_{-0.034} \times 10^{-4}$ has been measured and it is in agreement on a 1σ level with the previous measurement done by Bergmann using a pair of Timepix detectors. P_{KK} in electron capture decay of ^{54}Mn has been measured for the first time using hybrid pixel detectors, in our case with Timepix3. The measured $P_{KK} = (3.93 \pm 0.44) \times 10^{-4}$ with the systematic error of $\Delta_{sys}(P_{KK}) =^{+0.25}_{-1.11} \times 10^{-4}$. While coming with large errors, it agrees very well with previous measurements. To reduce the systematic unertainty, triple coincidences could be searched for in the data of ^{54}Mn and ^{65}Mn, thus reducing the amount of possibilities to consider. Moreover, the additional peak appearing in the time difference spectra for ^{54}Mn and ^{65}Mn, which was explained by drift time effects might provide means to separate signal from background. Therefore, however, the time spectrum shape needs to be reproducible in simulation.

Bibliography

[1] B. Bergmann. *Detection and separation of x-rays, neutrons and charged particles using hybrid pixel detectors.* PhD thesis, 2019.

[2] B. Bergmann. Application of a time-resolving x-ray pixel detector in the detection of coincident fluorescence emissions after double k-shell vacancy production in the electron-capture decay of ^{55}fe, 2012.

[3] E. P. Kanter, I. Ahmad, R. W. Dunford, D. S. Gemmell, B. Krässig, S. H. Southworth, and L. Young. Double k-shell photoionization of silver. *Phys. Rev. A*, 73:022708, Feb 2006.

[4] H. Primakoff and F. T. Porter. Atomic excitation and ionization accompanying orbital electron capture by nuclei. *Phys. Rev.*, 89:930–937, Mar 1953.

[5] B. Bergmann, T. Michel, A. Surzhykov, and S. Fritzsche. Angular correlation function of the hypersatellite-satellite x-ray cascade following k-shell electron capture of ^{55}Fe. *Phys. Rev. C*, 94:014611, Jul 2016.

[6] H. J. Nagy and G. Schupp. Double k-shell ionization in the electron capture decay of ^{54}Mn. *Phys. Rev. C*, 30:2031–2035, Dec 1984.

[7] M. M. Hindi, C. A. White, and R. L. Kozub. Double k-shell ionization probability in ^{54}Mn. *Phys. Rev. C*, 68:014306, Jul 2003.

[8] H. J. Nagy and G. Schupp. Double k-shell ionization in the electron capture decays of ^{65}Zn. *Phys. Rev. C*, 27:2887–2892, Jun 1983.

[9] R. L. Intemann. Double k-shell ionization in electron capture decay. *Phys. Rev. C*, 31:1961–1964, May 1985.

[10] D. Mitra, M. Sarkar, D. Bhattacharya, and L. Natarajan. Satellites, hypersatellites and rae from ti, v, cr, mn and fe in photoionisation. *X-Ray Spectrometry*, 37(6):585–594, 2008.

[11] lnhb.fr, laboratoire national henri becquerel, fe-55 table. `http://www.lnhb.fr/nuclides/Fe-55_tables.pd`. Accessed: 2022-12-30.

[12] T. Michel, B. Bergmann, Jürgen Durst, Mykaylo Filipenko, Thomas Gleixner, and Kai Zuber. Measurement of the double k-shell vacancy creation probability in the electron-capture decay of ^{55}Fe with active-pixel detectors. *Phys. Rev. C*, 89:014609, Jan 2014.

[13] M. C. Chon and J. Law. Probability for k- and l-vacancy creation in electron-capture decay. *Phys. Rev. A*, 50:1372–1376, Aug 1994.

[14] M. H. Biavati, S. J. Nassiff, and C. S. Wu. Internal bremsstrahlung spectrum accompanying $1s$ electron capture in decay of fe^{55}, cs^{131}, and tl^{204}. *Phys. Rev.*, 125:1364–1372, Feb 1962.

[15] J. G. Pengra and B. Crasemann. Energy spectrum of atomic electrons ejected in electron-capture decay of fe^{55}. *Phys. Rev.*, 131:2642–2648, Sep 1963.

[16] lnhb.fr, laboratoire national henri becquerel, mn-54 table. `http://www.lnhb.fr/nuclides/Mn-54_tables.pdf`. Accessed: 2022-12-30.

[17] H. Lancman and J. M. Lebowitz. Internal bremsstrahlung accompanying the electron-capture decay of mn^{54}. *Phys. Rev.*, 188:1683–1685, Dec 1969.

[18] lnhb.fr, laboratoire national henri becquerel, zn-65 tabl. `http://www.lnhb.fr/nuclides/Zn-65_tables.pdf`. Accessed: 2022-12-30.

[19] Medipix collaboration. `https://medipix.web.cern.ch/`. Accessed: 2022-11-30.

[20] Advacam flip-chip bump-bonding. `https://advacam.com/service/flip-chip-bonding`. Accessed: 2022-12-30.

[21] P Burian, P Broulím, M Jára, V Georgiev, and B Bergmann. Katherine: ethernet embedded readout interface for timepix3. *Journal of Instrumentation*, 12(11):C11001, 2017.

[22] J. Jakubek. Precise energy calibration of pixel detector working in time-over-threshold mode. *Nuclear Instruments and Methods in Physics Research Section A: Accelerators, Spectrometers, Detectors and Associated Equipment*, 633:S262–S266, 2011. 11th International Workshop on Radiation Imaging Detectors (IWORID).

[23] Root framework. `https://root.cern`. Accessed: 2022-11-30.

[24] S. Spannagel, K. Wolters, D. Hynds, N. Alipour Tehrani, M. Benoit, D. Dannheim, N. Gauvin, A. Nürnberg, P. Schütze, and M. Vicente. Allpix2: A modular simulation framework for silicon detectors. *Nuclear Instruments and Methods in Physics Research Section A: Accelerators, Spectrometers, Detectors and Associated Equipment*, 901:164–172, 2018.

[25] About allpix^2. `https://project-allpix-squared.web.cern.ch/project-allpix-squared/page/about/`. Accessed: 2022-11-30.

[26] Allpix^2 manual. `https://project-allpix-squared.web.cern.ch/usermanual/allpix-manual.pdf`. Accessed: 2022-12-30.

[27] B. Bergmann, M. Pichotka, S. Pospisil, J. Vycpalek, P. Burian, P. Broulim, and J. Jakubek. 3d track reconstruction capability of a silicon hybrid active pixel detector. *The European Physical Journal C*, 77(6):421, Jun 2017.

[28] J.P Briand, P Chevalier, A Johnson, J.P Rozet, M Tavernier, and A Touati. Experimental determination of the energy of k hypersatellite lines for various elements. *Physics Letters A*, 49(1):51–53, 1974.

[29] M. H. Chen. Auger transition rates and fluorescence yields for the double-k-hole state. *Phys. Rev. A*, 44:239–242, Jul 1991.

[30] M. Kavčič, M. Budnar, and J.L. Campbell. A database for kl ionization satellites in pixe. *Nuclear Instruments and Methods in Physics Research Section B: Beam Interactions with Materials and Atoms*, 196(1):16–24, 2002.

List of Figures

List of Tables